Masterproef 2017-2018

Gas temperature and vibrational temperature in a pulsed N_2 microwave plasma: a combined experimental and computational study to explore non-equilibrium conditions

Senne Van Alphen

Promotor: Prof. Dr. Annemie Bogaerts

M.m.v. Vincent Vermeiren & Tom Butterworth

Masterproef ingediend tot het bekomen van de graad van Master in de Chemie

Faculteit Wetenschappen

Departement Chemie

DIFFER
Dutch Institute for
Fundamental Energy Research

Universiteit
Antwerpen

Acknowledgement

The completion of this thesis could not have been possible without the participation and assistance of so many people. First of all I want to thank my promotor, Annemie Bogaerts, for not only providing a very interesting topic for the thesis, but also giving me the opportunity to complete this thesis in a collaboration with the Dutch Institute of Fundamental Energy Research, which was an amazing experience. While being one of the busiest persons I've met, she still manages to spare a lot of time, to discuss results, aid the research or to just pass by to see if everything is alright. During my stay in Eindhoven, everybody in DIFFER contributed in some way to the completion of this thesis. Especially Gerard, Alex, Dirk ,Theo and Qin provided useful help and assistance for the experimental side of the thesis. Special thanks go to Tom, for supervising me, sharing his knowledge and keeping me from breaking any expensive lab equipment during my experiments. For the modelling side, I could also count on a competent supervisor. Special thanks to Vincent for helping me a lot with the 0D model, to educate me with his modelling knowledge and to even spare vacation time to help me completing the thesis. Last but not least I want to thank my friends and family. My friends for distracting me (sometimes too long) from work and showing sincere interest and assistance and my family for the unconditional help and guidance they provided me. My most sincere gratitude goes to my parents for giving me the opportunity to even start studying.

Wetenschapspopulariserende abstract

Het smelten van de poolkappen, het stijgen van de zeespiegel, … de opwarming van de aarde dreigt een enorme impact te hebben op al het leven op Aarde. Om deze ecologische ramp te vermijden wordt men wereldwijd gedwongen het gebruik van fossiele brandstoffen zoveel mogelijk in te perken. Zo dient ook de chemische industrie zijn energie verbruik grondig te evalueren daar de sector nog te veel steunt op zeer energie-intensieve processen zoals het Haber-Bosch proces. Dit proces haalt stikstof uit de lucht en zet dit om tot de chemische componenten voor de productie van kunstmest. Hoewel het proces absoluut noodzakelijk is voor de wereldwijde productie van kunstmest, verbruikt het tot 2% van alle energie die op aarde geproduceerd wordt, wat het een zeer milieuvervuilend proces maakt. Plasmatechnologie kan echter een alternatief bieden dat in staat is op groene elektriciteit van windmolens of zonnepanelen te werken. In deze thesis worden zowel experimenten als computersimulaties uitgevoerd om een beter inzicht te krijgen hoe plasmaprocessen werken en optimaal kunnen worden uitgevoerd om op een milieuvriendelijke manier kunstmest te kunnen maken van stikstof van uit te lucht.

Samenvatting

Met de opwarming van de aarde in het vooruitzicht, dringt de noodzaak zich op om onze afhankelijkheid van fossiele brandstoffen op een zo kort mogelijke termijn af te bouwen. Een zeer belangrijke stap hierin schuilt in het ontwikkelen van groene alternatieven voor energie-intensieve chemische processen. Het Haber-Bosch proces, dat meer dan 130 miljoen ton ammonia per jaar produceert door middel van chemische stikstof (N_2) fixatie, is verantwoordelijk voor ~1-2% van het wereldwijde energieverbruik, wat het een van de meest milieuvervuilende chemische processen maakt. Plasma technologie is echter in staat een groen, elektriciteit-gedreven alternatief te bieden voor het Haber-Bosch proces. Het feit dat plasma's kunnen worden aangedreven door groene elektriciteit en geen werkcondities bij hoge druk of temperatuur vereisen, maakt lage temperatuurs-plasma's een veelbelovende technologie in de ontwikkeling van een duurzame chemische industrie. Het onderzoek in deze thesis maakt gebruik van een gepulst microgolf plasma om N_2 te dissociëren. Het breken van de sterke N≡N binding is namelijk de belangrijkste en moeilijkste stap in het N_2 fixatie proces. In plasma's wordt N_2 vibrationeel geëxciteerd, zodat de binding zelfs bij relatief lage temperaturen kan breken. Door een gecombineerde experimentele en gemodelleerde studie van de vibrationele temperatuur en gas temperatuur in een gepulsd microgolf plasma, worden de onderliggende mechanismen van een gepulst plasma regime onderzocht. Het onderzoek toont aan dat een gepulst plasma relaxatie processen die werken op een lange tijdschaal en energie verloren doen gaan aan het opwarmen van het gas, verhindert. Bovendien wordt aangetoond dat boven een zeker puls frequentie en pulslengte (i.e., pulsfrequenties boven 7000 Hz en pulslengtes boven 400 µs), dit voordeel verdwijnt. De conversies die bereikt worden in de onderzochte gepulste microgolf reactor, liggen rond de 2 %, wat veelbelovende waarden zijn t.o.v. andere plasma-gebaseerde N_2-fixatie technieken. Hoewel de resultaten van deze thesis nog verre van vergelijkbaar zijn met het sterk geoptimaliseerde Haber-Bosch proces, toch brengt deze studie de wetenschap een stap dichter in het begrijpen en het ontwikkelen van N_2-fixatie door lag-temperatuurs-plasma's.

Summary

Given the major environmental concerns associated with fossil fuels, a short-term transition from a carbon-based energy economy to a sustainable one is essential. A key step concerning this transition exists in providing green alternatives for energy intensive chemical processes. The Haber-Bosch process, which produces more than 130 million tons of ammonia per year through chemical nitrogen (N_2) fixation, is responsible for ~1-2% of the world's total energy consumption, contributing significantly to the chemical industry's environmental impact. Electricity-driven plasma processes are considered to be very attractive candidates for a green Haber-Bosch replacement. Working at ambient conditions and being able to use green electricity as an energy supply, plasma technology delivers a cutting-edge innovation in the electrification of the chemical industry. This thesis presents a pulsed microwave (MW) plasma for achieving dissociation of pure N_2. Breaking the strong N≡N bond is the most important step of the N_2 fixation process and is achieved by activating the N_2 through vibrational excitation. Performing both experimental and modelling studies of the vibrational and gas temperature in a pure N_2 plasma, the advantages and underlying mechanisms of a pulsed plasma regime are investigated. Results show that long time scale relaxation processes, which lose energy to gas heating, are inhibited by supplying the power in a pulsed manner. It is also observed that above a certain pulse frequency or pulse width (i.e., pulse frequency above 7000 Hz and pulse length above 400 μs), this advantage starts to fade away. The conversion, achieved in the presented pulsed MW, reactor is calculated to be around 2 %, which makes this reactor competitive with other plasma-based N_2 fixation techniques. While the performances presented in this thesis are far from comparable to the highly optimised Haber-Bosch process, the study helps opening the way to a better understanding and development of N_2 fixation through low temperature plasma technology.

Table of contents

1.Introduction

1.1 This century's greatest energy problem

Fossil fuels shape an enormous part of our modern-day society. Because of their availability, usability and high energy density, fossil fuels played a major role in the rapid, unprecedented technological development of the past century. Nowadays fossil fuels are still the principal energy source humankind is dependent upon, providing more than 80% of our present energy needs. However, their use unfortunately comes with a great cost: burning fossil fuels leads to the emission of enormous amounts of the greenhouse gas CO_2.

Driven largely by economic and population growth, the anthropogenic greenhouse gas emissions are now higher than ever. This has led to atmospheric CO_2 concentrations above 400 ppm, which is unprecedented in at least the last 800,000 years.[1] Content analysis of air bubbles captured in ice more than hundreds of thousands of years ago have shown that the atmosphere's CO_2 concentration fluctuated a lot throughout the centuries. However, as visible in figure 1, never did it surpass the currently measured concentration values.[2]

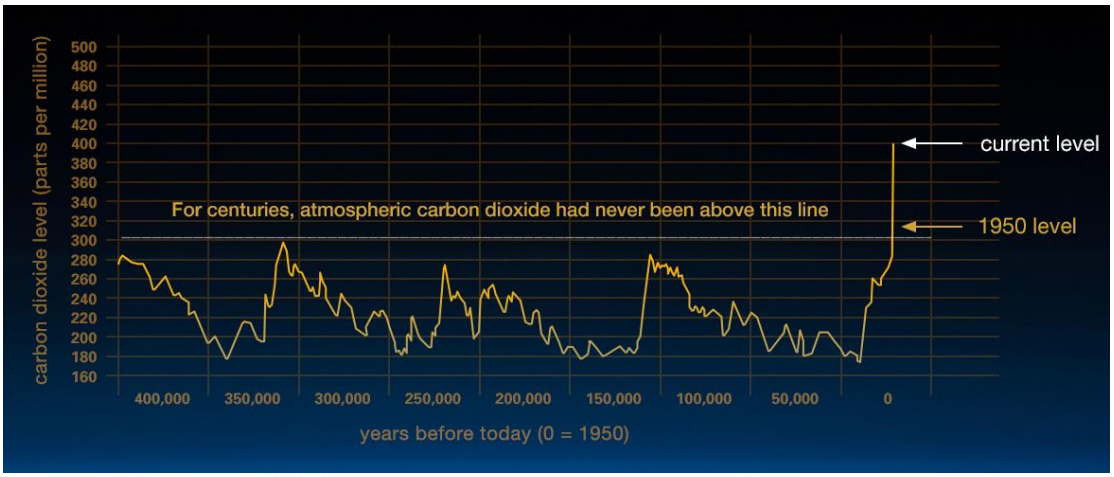

Figure 1: Atmosphere's CO_2 concentration in ppm throughout the centuries, measured from air bubbles captured in ice.[2]

Recent technological advances made it clear that this increase in atmospheric greenhouse gasses threatens the natural balance of the Earth's ecosystem.[2] Global warming is undoubtedly happening and the role that greenhouse gasses play in it is well understood. Greenhouse gasses such as CO_2 absorb heat, which is constantly radiating from the Earth's sunlight absorbing

surface. The heat energy, absorbed by these molecules, is emitted again homogeneously in all directions, having the possibility of being sent back again to the Earth's surface.[1] This entrapment of heat inside the Earth's atmosphere is called the "greenhouse effect", and is in its origin a natural process of vital importance: without it, the Earth's average temperature would be -18 °C instead of the current 15°C. However, the enormous anthropogenic emission of greenhouse gasses is causing this natural effect to escalate, disrupting the natural balance of the atmosphere's temperature.[3]

Consequences of the Earth's rising temperature are well known, the most infamous one being the melting of the polar caps. Melting the water stored in the Arctic icecaps, as well as the expansion of seawater as it warms up, is causing a dangerous rise in sea level. Especially coastal regions will bear these consequences in the form of floods and a general decrease in inhabitable space. But the destruction of the arctic ecosystem and a rise in sea level are not the only consequences of global warming. The resulting disruption imbalances are threatening to be so radical that enormous floods, storms, as well as extreme heat and drought, will occur more frequently and be more extreme all over the world. The disastrous consequences of global warming affect every single inhabitant of our planet, which makes it one of the primary challenges of the 21st century.[1]

The past decades, the common understanding has been developed that global warming represents a severe threat to our current society and future generations in general. Many political efforts have been done to reach an agreement about lowering the greenhouse gas emissions. Those negotiations recently led to the Paris Agreement, in which 174 countries began adopting their own legal system. The Paris Agreement aims to limit global warming "well below 2 °C" compared to pre-industrial levels and to pursue efforts to limit the temperature increase to 1.5 °C. Adhering to this ambitious plan means achieving zero emission some time between 2030 and 2050, which demands the massive use of fossil fuels to be addressed quickly. A short-term transition from a carbon-based energy economy to a sustainable one is therefore essential.[3]

As human technology is the cause of global warming, human technology can also be the solution. The recent developments in renewal energy technology seem promising for replacing fossil fuels by green electricity on a global scale. Especially photovoltaic panels for capturing solar energy and wind turbines for converting wind energy are experiencing a rapid growth in development and application.[4] While these energy resources have the advantage of being based on environmentally clean, nearly infinite energy supplies, they have an unfortunate drawback: their intermittency. As one has no control over the energy provided by the sun or the wind, there

is a clear mismatch between the supply of renewal energy and the peak in energy consumption. For example: while the mean peak of solar energy production is located around 12 o' clock, the main peak in energy consumption lies around 6 p.m. This temporal mismatch, as well as fluctuations because of the weather dependency of renewal energy sources, make renewal electricity too unreliable for our modern-day energy demands. Furthermore, such unstable supply of electricity can present major stability problems for the power grid, as the renewable power capacity increases. The future energy landscape is thus in need of a technology that can efficiently store and transport peak energy and stabilise the power grid, while being inherently flexible to manage the intermittent energy supply of renewal electricity. Such a flexible, yet efficient process can be provided by plasmas. Plasma technology delivers the interesting possibility to convert (renewable) electricity into fuels and chemicals, which are much more easily storable energy resources.[5] In these conversion applications, plasmas use electric energy to convert stable, nearly inert gas molecules like CO_2 and N_2 to useful products, literally creating chemicals out of thin air. This revolutionary process delivers an answer to the intermittency of green electricity sources like solar and wind energy, as it gives the opportunity to create storable energy sources on times of peak energy supply, when there is literally an excess of electric energy.[6] The technology is inherently flexible, as plasmas deliver a so-called "turnkey" process, being able to easily be switched on and off following the energy supply. Plasmas are thus a great enabler for a future of sustainable energy, opening the way for the complete electrification of the energy and chemical industry.[7]

1.2 Plasma, shaping the future energy landscape

Plasmas, often referred to as the fourth state of matter, are (partially) ionised gasses. Plasmas thus distinguish themselves from normal gasses by containing significant amounts of charged species, like ions and electrons, as well as reactive species, like radicals, and excited species. This last kind is responsible for a very distinctive feature of a plasma: excited species in the plasma have the possibility to return to a lower energy state, by emitting light. The wavelength of this light is characteristic to the excited species energy levels, resulting in distinctive light colours for a certain gas composition. By being composed of various reactive compounds interacting with each other and the environment, plasmas are a complex but chemically very interesting state.[8]

Although more than 99 % of the visible universe is in the plasma state, plasmas are less common here on Earth. The most famous close-to-Earth plasma is our Sun, being a 1.39 million km diameter ball of mostly hydrogen plasma, sending its emitted light across our solar system. Closer to the Earth's surface, natural plasmas manifest themselves in the form of lightning, Auroras or Saint-Elmo's fire. Besides these natural plasma-based processes, the major phenomenon responsible for creating plasmas on the Earth's surface is human technology. Neon lights, fluorescence tubes or plasma TV screens are a few examples of the many everyday uses of plasma technology. Generally, plasmas are made by giving a sufficient amount of energy to a gas, in order to ionize its atoms or molecules. This energy can be given to the plasma by simply heating it: warming up the gas until it spontaneously dissociates, as done in fusion plasmas. These thermal plasmas operate at millions of degrees to mimic the conditions of the Sun in order to realize nuclear fusion as a future energy source.[8] However, in most of the recent plasma applications, like using green electricity to convert gas into fuels and chemicals, the plasma operates at much lower temperatures, even close to room temperature. The aim of these plasmas is not to heat the gas as a whole, but to selectively heat the electrons of the plasma. In the end it will be the electrons that activate the gas molecules for conversion, so supplying energy only to them will be the most energy-efficient approach. Plasmas following this method are called non-equilibrium plasmas, as there exists a thermal nonequilibrium between the highly energetic electrons on the one hand (typically with energy of a few eV, i.e., several 10 000 K) and the gas molecules on the other hand (virtually at room temperature up to a maximum of a few 1000 K).[8] Such a non-equilibrium can be achieved in its most simple way by two parallel plates with a potential difference between them. Electrons from gas molecules between the plates will be accelerated by the electric field between the plates, inducing collisions that ionize gas molecules. These ionization reactions produce more ions and electrons, resulting in a partially ionised gas that we call a plasma. The cascade formation of charged species by ionisation will ultimately make the gas conductive and create a discharge between the plates. Besides ionization reactions, also excitation and dissociation reactions are caused by collisions between species in the plasma. Excitation will excite species to higher energy levels, while dissociation splits molecules, often creating radicals that make plasmas chemically reactive.[8] This chemically active plasma that ends up between the plates is achieved by nothing more than applying electrical energy to a gas. This explains why plasmas are potentially interesting in combination with renewable electricity.[9]

1.3 Nitrogen fixation

1.3.1 Historical context

An important application of green energy plasma-based gas conversion lies in N_2 fixation. Nitrogen is a crucial element for the growth of any living organism, since it is an essential part of amino acids and nucleotides, which lead to the formation of proteins, DNA and RNA, the building blocks of all life on Earth. With an atmosphere of 78% nitrogen gas (N_2), the Earth has an abundance of this vital element, but unfortunately atmospheric N_2 is hardly accessible to most living beings. The extremely stable N≡N bond of N_2 requires a lot of activation energy to be broken, which prevents most organisms to incorporate atmospheric N_2 in their nitrogen metabolism. To make this enormous source of nitrogen accessible to organisms like plants, the N_2 molecule must be broken up and chemically bonded to oxygen or hydrogen through a process called N_2 fixation.[9]

Nature has a few means to break this highly stable bond, as N_2 fixation occurs spontaneously on Earth by specialised N_2 fixing microorganisms or by the high energy present in a lightning strike.[10,11] This natural N_2 conversion into ammonia and NO_x is responsible for 297 million tons of N_2 being fixated each year.[10] However, the increased global population has intensified agriculture past the point that this amount of biologically fixed N_2 is sufficient for raising the required food plants.

This issue already became apparent in the beginning of the 20th century, at which point people put a lot of effort in developing a chemical process to fix atmospheric N_2 gas. In 1903, a plasma-based approach was considered for the first time by Birkeland and Eyde, who developed a thermal arc furnace to convert air into nitrogen oxides.[12] Unfortunately, the thermal nature of the arc furnace plasma made the process little appealing for industrial use, as the energy efficiency of the NO_x formation was very low, operating at these high temperatures. In 1908 the Haber-Bosh process was developed, a process that to this day remains the conventional way to fix N_2.[10] In this process, ammonia (NH_3) is synthesized from N_2 and H_2 gas using iron as a catalyst in an environment of relatively high temperature (400-500°C) and high pressure (150-250 bar). The Haber-Bosch process nowadays provides 135 million tons of fixed N_2 each year, indirectly feeding 40% of the world population through fertilizer production.[10] Unfortunately, the process consumes almost 2% of the world's total energy production, emitting 300 million

metric tons of CO_2 and utilizing 3-5% of the natural gas output each year. The process was significantly optimised the past 100 years, essentially reaching its theoretical optimisation limits.[13] As a result, the environmental impact of N_2 fixation processes can only be improved by searching for approaches which are very different from the Haber-Bosch process. [13]

Among several solutions, revisiting the plasma-based process seems very promising. Using our current knowledge of non-equilibrium plasmas, high energy electrons can forcefully interact with the stable nitrogen bond, while the bulk gas remains close to room temperature. Losing little energy to heating the bulk gas, the poor energy efficiency of the Birkeland and Eyde thermal plasma is avoided. Reconsidering the plasma-based approach seems worthwhile, as it harmonizes greatly with a future of renewal electricity and the previously discussed electrification of the chemical industry. Furthermore, the theoretical limit of the energy consumption of nitrogen oxidation by non-equilibrium plasmas is 2.5 times lower than that of the Haber-Bosch process,[13] giving it an edge over the classical Haber-Bosch process when it is optimised towards this limit. Also the fact that plasmas operate at ambient temperature and pressure and only require air and not hydrogen as raw material, makes plasma-based processes even more promising.[14] The main future for this technology is deemed to be, contrary to the Haber-Bosch process, in modular, small-scale reactors for localized production of fertilizers from air using renewal electricity. Especially local farmers in regions where wind and solar resources are well-supplied but under-used, could really benefit from this local fertilizer production.[9,15]

1.3.2 Plasma-based N_2 fixation

The plasma-based NO_x formation has already been tested in different kind of plasma reactors.[9] Three reactors are most common in non-equilibrium plasma-based gas conversion application, i.e. the dielectric barrier discharge (DBD) reactor[16], the microwave (MW) reactor[17] and the gliding arc (GA) reactor[18]. The MW reactor, which doesn't use electrodes but MWs to generate a plasma, delivers the best results at reduced pressure, yielding an energy cost of 0.3 MJ/mol for an NO_x yield of 14 %.[17] Second in place is the gliding arc reactor, with a 2% NO_x yield and 2.8 MJ/mol energy consumption.[18] The reason why MW discharges (and also GA discharges) yield the most promising result is because they create significant vibrational excitation of N_2. As revealed by recent computer modelling, the most efficient way of breaking the N≡N bond is not achieved by direct electronic excitation with high energy electrons, but by gradually exciting the vibrational states of N_2.[19] As shown in figure 2, vibrational excitation is the

dominant reaction type when electrons have an energy around 1 eV, typically obtained at reduced electric fields lower than 100 Td. This is the characteristic operating region of a MW or GA reactor.[19] Subsequently, theses vibrationally excited N_2 molecules collide with each other and cause vibrational-vibrational relaxation (VV relaxation), exchanging their vibrational energy. This causes one of the colliding molecules to end up populating a higher vibrational energy level. Going through a series of these vibrational relaxation collisions, molecules can thus gradually populate higher vibrational energy levels, a process which is often referred to as vibrational ladder climbing.[19] Through this vibrational ladder climbing, an N_2 molecule eventually reaches energy levels close to the bond dissociation energy of the N≡N bond (9.765 eV), facilitating the breakage of the bond. Vibrational ladder climbing will thus help to "climb over" the reaction energy barrier of the nonthermal Zeldovich mechanism ($O + N_2(v) \rightarrow NO + N$), the fixation reaction that breaks the N≡N bond and reacts with atomic oxygen to form NO. This NO can react further by oxidizing it to NO_2.[9,19]

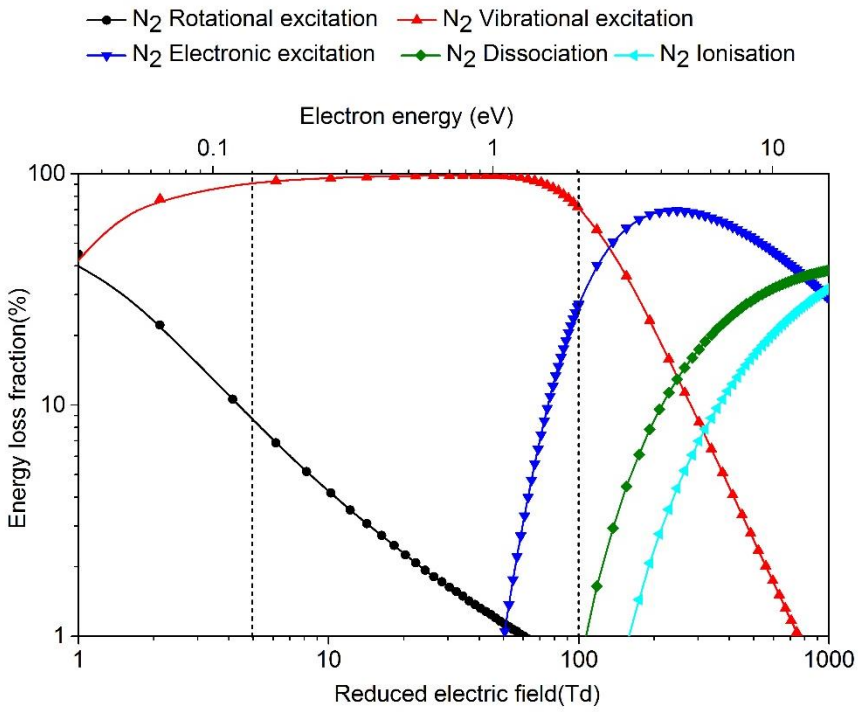

Figure 2: Fraction of electron energy transferred to different channels of excitation, ionization and dissociation of N_2, as a function of the reduced electric field (bottom x-axis) and electron energy (top x-axis).[19]

However, besides the VV relaxation process to gain vibrational energy and climb up the vibrational ladder, there also exists a collision mechanism for vibrational population to be lost. As a response to the non-equilibrium between vibrational and thermal energy caused by exciting vibrational states, vibrational-translational (VT) relaxation occurs.[19] This relaxation process causes the excited energy of N_2 to be transferred from vibrational to translational energy

upon collision with another species. This is deemed highly unfavourable, as the vibrational energy, which is required to overcome the reaction energy barrier, is lost to heating the gas. As revealed by computer modelling, this energy loss mechanism becomes more important at high gas temperature, on the order of several 1000 K.[19] By raising the temperature, the VT relaxation collisions will ultimately occur so frequently that the vibrational levels will be in complete thermal equilibrium with the gas temperature. Avoiding the temperature to rise and the vibration energy to thermalize is thus of very high priority in N_2 fixation through non-equilibrium plasmas.[20] One option to prevent the gas temperature from raising too high includes operating in a supersonic gas flow.[21] As a gas uses its own internal energy to accelerate supersonically, the gas cools itself, avoiding the vibrational levels to thermalize. An alternative option could be to supply the power source of the plasma, like the MWs of a MW plasma, in a pulsed manner, so time is provided for the plasma to cool down between pulses.[9] This last option is relatively easily to apply on a plasma setup and indeed looks very promising for N_2 fixation, but more fundamental research is needed to fully exploit the advantages of powering the plasma in pulses. It is this pulsed system that will be the point of interest in this thesis.

1.4 Aim of this research

The need for a transition to a sustainable energy economy, as well as the enormous environmental impact of the Haber-Bosch process, makes a revisit of the plasma-based process for N_2 fixation very interesting. With the current knowledge of the vibrational excitation of N_2 in non-equilibrium plasmas, the application of pulsed plasmas seems promising to prevent vibrational energy levels from thermalizing. However, the exact behaviour of the non-equilibrium between vibrational and thermal energy in a pulsed plasma is not yet well understood. As the vibrational ladder climbing mechanism puts an enormous emphasis on the effect of VT and VV relaxation, a fundamental study of the behaviour of these plasma mechanisms in a pulsed regime can be very interesting. To address these fundamentals of plasma-based N_2 fixation through vibrational excitation, a combined experimental and computational study of a pulsed N_2 MW plasma will be the subject of this master thesis.

2.Experimental methodology

2.1 Vibrational Raman spectroscopy

To observe vibrationally excited N_2 species in the plasma, vibrational Raman spectroscopy is conducted. The basics of the theory underlying this spectroscopic technique are explained in this section and are based on information found in the work of Long.[22]

2.1.1 The Raman effect

Raman spectroscopy is a spectroscopic technique used to observe low frequency modes of molecules, like the vibrational modes of N_2. This is achieved by analysing light that has scattered inelastically on the excited molecule. Inelastic light scattering is a scattering process in which an energy transfer takes place between the scattered light and the molecule, causing the incident and the scattered light to be observed at different wavelengths. This concept is usually described via a virtual state, which is a short-lived state with a well-defined energy that is not associated with any physical state of the molecule. During Raman spectroscopy, such a virtual state is excited during the interaction of an incoming photon and a molecule. Reaching this virtual state presents the molecule three potential outcomes, as shown in the Jablonski diagram in figure 3. In the first option, the molecule relaxes back to its original state and emits a photon of equal energy to the incident photon. This transition represents elastic scattering, also known as Rayleigh scattering. During Rayleigh scattering, no energy is transferred between the photon and the molecule. In the second option, the molecule relaxes to a real non-virtual state, higher in energy than the state it was originally in. During this relaxation a photon is emitted with a lower energy than the initial incident photon. The part of the energy that was lost during scattering resides in the molecule, leaving it in the vibrational/rotational excited state corresponding to the residing energy. This inelastic scattering event is called Stokes scattering. Analysing the energy of the photon that was emitted when the molecule relaxed from its virtual state yields information about the initial vibrational state of the molecule. For the third option, the molecule relaxes to a state with lower energy than it was initially in, again by emitting a photon. The emitted photon now has higher energy than the incident one, again leaving the molecule in a corresponding vibrational-rotational state. This last option, Anti-Stokes

scattering, is the subject of fewer research, as this type of scattering requires the initial molecules to already populate a higher vibrational-rotational state above the ground state.

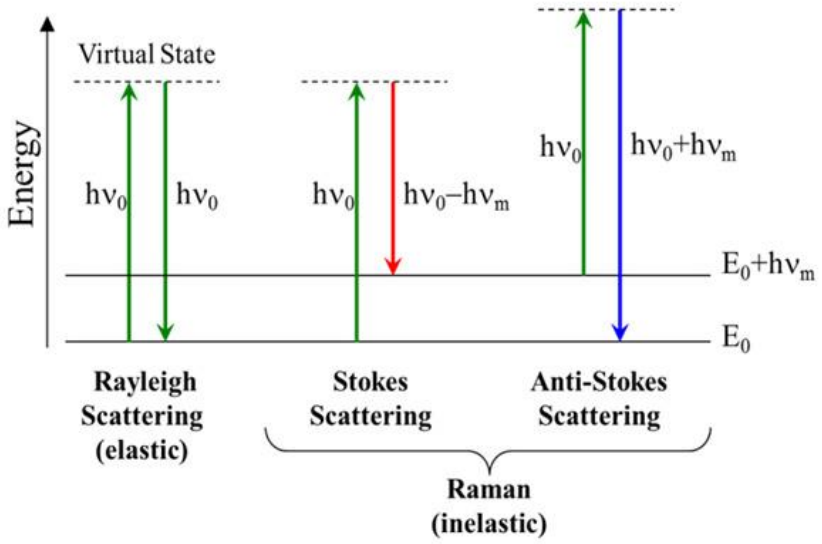

Figure 3: Jablonski diagram, schematically showing the three different potential ways light can scatter upon interaction with matter: Rayleigh scattering, Stokes scattering and Anti-Stokes scattering.

This energy level-based description of Raman spectroscopy visualises neatly the useful information that Stokes scattering can deliver for non-equilibrium studies of plasma: Analysing the energy of an inelastically scattered photon directly yields information about the vibrational state of a molecule before scattering. As the selection rule for the vibrational quantum number in vibrational Raman spectroscopy is $\Delta v=1$, every excited vibrational state will be represented by a signal at one distinct wavelength. The intensity of this signal is proportional to the population density. This intensity of the scattered radiation is not homogeneously distributed but is a function of the angles at which it is detected. It is advantageous to collect the scattered radiation perpendicular to the laser beam where the cross section is the largest and where there is the least chance of collecting stray light. Other ways to improve the intensity is by careful selection of the excitation wavelength. Both the cross section of the virtual absorption and the power of the Raman radiation are proportional to $1/\lambda^4$ and thus benefit from low frequency lasers. This justifies the choice of a 532 nm wavelength laser.

2.2.2 Data Analysis

Rotational and vibrational temperature

To observe the effect of a pulsed power supply on the vibrational non-equilibrium, the non-equilibrium in a MW plasma needs to be quantified by experimental measuring markers. The definition of these non-equilibrium quantities instinctively arises when examining how a non-equilibrium is formed. In thermal equilibrium, the distribution of energy within the translational, rotational and vibrational modes is described by the Boltzmann distribution. The occupancy of a generic state i can then be calculated as:

$$\frac{n_i}{N} = \frac{g_i exp\left(-\frac{E_i}{k_b T_{gas}}\right)}{\sum_i g_i exp\left(-\frac{E_i}{k_b T_{gas}}\right)} \quad (1)$$

where N is the total number of molecules, E_i is the energy of the i_{th} state g_i is a statistical weight describing the degeneracy of the i_{th} state, k_b is the Boltzmann constant and T_{gas} is the gas temperature. Vibrational non-equilibrium means that the energy distribution of the translational, rotational and vibrational modes is no longer described solely by equation 1, which uses a single T_{gas} temperature. As a unique temperature loses its ability to describe the thermodynamic state of the gas, two new temperatures are defined, the vibrational temperature (T_v) and rotational temperature (T_r). T_v and T_r, together with T_{gas}, represent to which extent the energy is distributed unequally between these degrees of freedom. These temperatures are thus a quantification for the existing non-equilibrium. In pulsed MW plasmas, vibrational non-equilibrium is achieved, creating a clear distinction between T_v and T_{gas}. T_v is defined using the energy and the population density of the first vibrational level (E_1 and n_1) and the population of the vibrational ground state (n_0):

$$T_v = \frac{E_1}{k_b \ln\left(\frac{n_1}{n_0}\right)} \quad (2)$$

T_r, on the other hand, does not display this non-equilibrium in significant time scales, which creates the potential to use T_r as a good estimation for T_{gas}.[23]

The Raman spectrum

As described, the extent to which non-equilibrium can be established in a MW plasma depends on the balance between T_v and T_{gas} (with the latter estimated by T_r). Both T_v and T_r can be extracted from a single Raman spectrum, since vibrational as well as rotational modes are

observable through Raman spectroscopy. To obtain this information, the peaks of the spectrum need to be fitted, knowing that the intensity (I) of the scattered light can be written as:

$$I = (V_i, J, T_r) = CN\gamma_{V_i}(\nu_l - |\Delta\nu(V_i, J)|)^4 exp\left(-\frac{hcB_{V_i}J(J+1)}{kT_r}\right) \quad (3)$$

where C is a factor accounting for the overall collection efficiency of the diagnostics, N is the scatterer's number density, T_r is the rotational temperature, ν_l is the wavenumber of the incident laser radiation, $\Delta\nu(V_i,J)$ is the energy shift associated with the transition, and B_{Vi} and γ_{Vi} are the rotational constant and the polarizability of a molecule in the vibrational state V_i, respectively. For non-degenerate fundamental bands, the Raman shift for a given rotational quantum number J is equal to

$$|\Delta\nu(V_i, J)| \cong \nu_{vib} + \left(B_{V_i+1} - B_{V_i}\right)J(J+1) \quad (4)$$

Where ν_{vib} is the energy difference between the two vibrational levels involved in the transition.

Synthetic spectra are thus calculated using equation 3 for each detected peak. As shown in equation 3, the profile of a band is a function of the rotational temperature, which is considered to be constant for each of the vibrational states. The value for T_r thus results from fitting equation 3 to the different bands in the spectra, the other fitting parameter being the height of the peak. Each band profile, after being calculated with the fitted heights and T_r, is integrated to obtain a value which is proportional to the population of each vibrational level and to the collection efficiency of the apparatus. The relative (to ground state) populations are then calculated using:

$$\frac{n_\nu}{n_0} = \frac{1}{\nu+1}\frac{\int Q_\nu(\bar{\nu})d\bar{\nu}}{\int Q_0(\bar{\nu})d\bar{\nu}} \quad (5)$$

where n_0 and n_ν are the populations of the ground and of a vibrational level, respectively, and the integrals are calculated over the fitted band profiles $Q_0(\bar{\nu})$ and $Q_\nu(\bar{\nu})$. In the formula, the (ν+1) factor corrects for the dependence of the Raman scattering cross section on the vibrational quantum number. In conclusion, the fit outcomes are 1) the rotational temperature T_r and 2) the relative (to ground state) populations of the vibrational levels, which in turn allows to calculate the vibrational temperature T_v via equation 2. An example of an experimental Raman spectrum is provided by figure 4. This example is a spectrum measured halfway through the pulse where the plasma is already sufficiently excited to populate several higher vibrational levels. These vibrational transitions are clearly resolved as separate bands in the spectrum. The rotational transitions, however, are not individually visible in this spectrum, as the setup does not allow

to distinctively resolve rotational lines. Instead, the rotational lines are closely packed as a continuum around the vibrational transition, defining the broadness of the vibrational bands. From the fit of the spectra, which, as visible, agrees well with the data, the value of T_r is extracted, as well as the values for T_v and the population density by integrating the fitted bands.

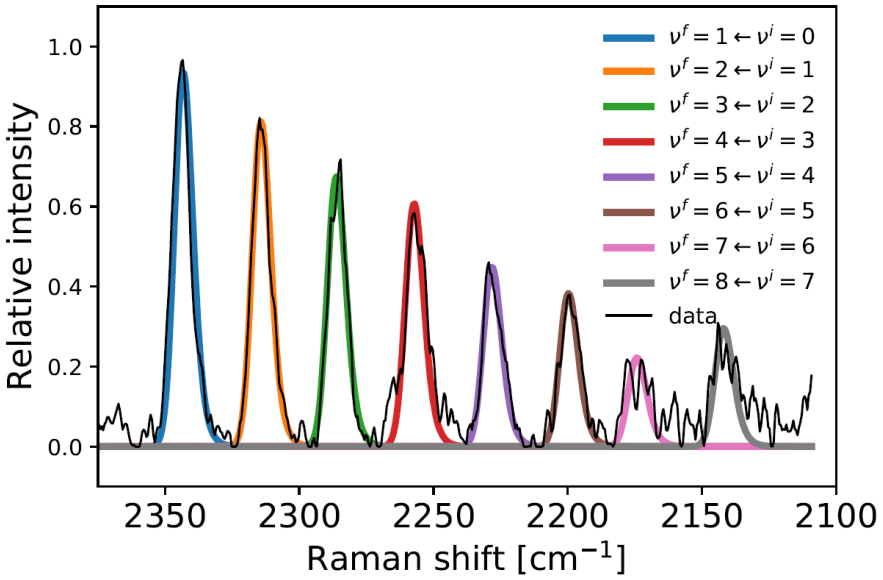

Figure 4: Example of a vibrational Raman spectrum (measured in a N_2 MW plasma at 25 mbar with a flow rate of 4 slm), showing the measured data, as well as the fitted transitions using equation 3.

2.2 Experimental setup

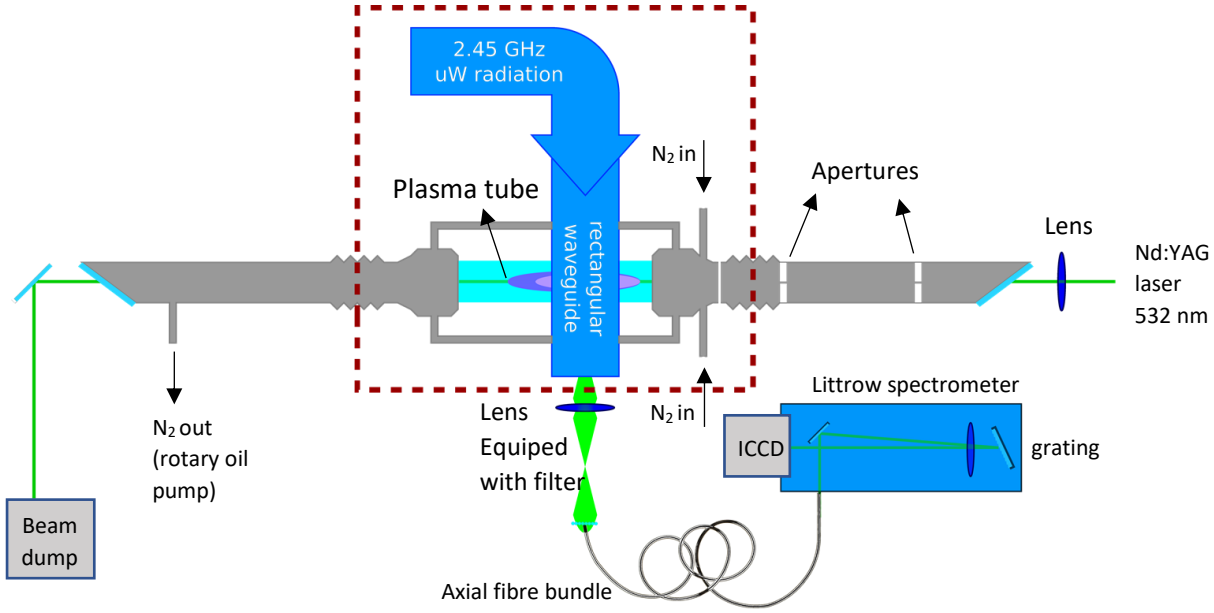

Figure 5: Schematic overview of MW plasma reactor and Raman set-up[12].

The experiments are conducted in a MW plasma reactor, depicted schematically in figure 5. In this reactor the plasma is generated in a 30 mm outer diameter quartz tube (plasma tube in figure 5), which is connected to two metallic pipes at both ends. The plasma tube is supplied with 4 slm of N_2 gas through two tangential injection nozzles in the upstream metallic pipe on the right. After passing through the plasma tube, gas is exhausted by a scroll pump connected to the downstream pipe on the left, keeping the gas pressure in the tube at 25 mbar. The plasma in the quartz tube is generated by exposing the gas to 2.45 GHz MW radiation. This is applied through a rectangular WR-340 waveguide surrounding the tube, forming a cavity with the exact right dimensions to create a standing wave of MW radiation in the tube. Three stub tuners inserted into the waveguide allow the impedance of the MWs to be tuned to match the plasma impedance and form a stable plasma. These knobs are tuned at the start of every experiment, to make sure the maximum amount of MW power is absorbed by the plasma.

As these experiments aim to investigate pulsed plasmas, the MW power will be applied in pulses. The signals to form this pulsed MW radiation are provided by a signal generator (Rigol LX1 2 channel DG1602Z). The generator sends periodic signals with a frequency of choice to the synthesizer of the MW source, which transforms the signal into four MW channels, each transporting ± 150 W of MW power. The waves in these channels are passed to the amplifier,

which amplifies the MWs by means of coaxial cables and eventually sends them to the waveguide.

The optical aspects of the experiment are provided by a Nd:YAG laser, frequency-doubled to give 6W output power in 20 ns pulses at 532 nm. The flash lamp as well as the Q-switch of the laser are also triggered by the previously mentioned Rigol LX1 signal generator, firing the laser at a frequency of 10 Hz through the vacuum tubes of the setup. Before reaching the plasma, the laser beam passes through a 1700 mm focal length lens, focusing it in the centre of the plasma, and through two apertures in the metal pipes, so stray light is reduced. Once in the plasma tube, scattered light from the laser is collected through a hole in the waveguide using an axial fibre bundle. Light is focussed on the bundle using a lens, equipped with a 550 nm AR longpass filter to further reduce stray light. After passing through the plasma and being scattered, the laser is sent to a beam dump. The collected scattered light is focussed by a 100 mm focal length lens onto the fibre bundle into a custom spectrometer, consisting of a spectral grating and iCCD camera in a Littrow configuration in an enclosed box (see figure 5). By rotating the grating, it is possible to observe a different part of the light spectrum in a spectral window of about 275 cm^{-1}. The light in this spectral window is focussed onto the iCCD camera (PI-MAX4:1024i), being intensified with a gain of 10 000 by the intensifier in the camera and accumulated over 9000 shots (15 minutes). These camera shots are also triggered by the previously mentioned signal generator. A delay generator (Stanford Instruments DG353 4 channel digital delay/pulse generator) manages the delay between all the trigger signals of the signal generator, so the firing of the laser, the imaging of the camera and the MW pulses are always synchronised.

3.Model description

Computational models provide very fundamental information about the kinetics in the plasma and can provide an answer to the general question "What are the underlying mechanisms of a certain plasma property?". Densities of any plasma species or trends in plasma processes are easily observed through computational models. Delivering this kind of valuable answers solely through experiments is time consuming, expensive and sometimes even impossible. Adding computational support to experimental results is thus without a doubt an added value, which is exactly the aim of this research. To achieve this, a zero-dimensional (0D) model is used. This model describes the evolution of the densities of the various plasma species through time, not through any space dimension, which is why it is called zero-dimensional. A 0D model thus describes all plasma parameters uniformly as being distributed in the considered volume, not taking into account plasma instabilities or transport processes due to diffusion, migration or convection.[19] This is a significant approximation, but provides the advantage of short calculation times and an overall uncomplicated physical model, allowing the use of a complex chemistry. A 0D model is thus the ideal tool to provide insight in the complex chemical interactions that exist in a plasma, without the need to describe difficult reactor configurations or flow patterns. Furthermore, the information that a 0D model provides about the plasma chemistry is a perfect starting point for future, more complex (1D, 2D or 3D) models.

3.1 Equations solved by the model

The 0D model used in this thesis is ZDPlasKin (Zero-Dimensional Plasma Kinetics solver). In this model the time evolution of the plasma species densities is calculated by balance equations, taking into account the various production and loss terms by chemical reactions. Such a balance equation of a species density is given by:[20]

$$\frac{dn_i}{dt} = \sum_j \left[\left(a_{ij}^R - a_{ij}^L \right) k_j \prod_l n_l^L \right] \quad (6)$$

in which n_i is the density of species i and a_{ij}^R and a_{ij}^L are the stoichiometric coefficients of species i on the right-hand (R) and left-hand side (L) of the reaction j. n_l is the density of species l, the reaction product on the left side of the reaction. k_j is the reaction rate constant of reaction j, which has the general form:

$$a_A A + a_B B\ (+\delta\varepsilon) \xrightarrow{k_j} a_c C + a_D D\ (+\delta\varepsilon)$$

in which A,B,C,D are the species and a_A, a_B, a_C, a_D their stoichiometric coefficients. δε represents the possible energy change during the reaction. The rate coefficients of these reactions are adopted from literature for the heavy particle reactions, whereas the rate coefficients for the electron impact reaction are calculated with a Boltzmann solver, BOLSIG+[24], built into ZDPlasKin. This Boltzmann routine calculates the Boltzmann equations for the electrons using a two-term approximation, yielding the electron energy distribution function (EEDF) as result. From the EEDF the mean electron energy and the different electron impact rate coefficients are obtained through the following equation:

$$k_j = \int_0^{+\infty} \sigma_j(\varepsilon)\, f_e(\varepsilon) \sqrt{\frac{2\varepsilon}{m_e}}\, d\varepsilon \qquad (7)$$

in which ε represents the electron energy, $\sigma_j(\varepsilon)$ the cross section of the j[th] electron collision reaction, $f_e(\varepsilon)$ the EEDF and m_e the mass of an electron (9,1094 10^{31} kg). The reaction cross sections $\sigma_j(\varepsilon)$ of the different elastic and inelastic collisions are adopted from literature.[25]

In this study, the time dependence of the model is converted to axial variation of the plasma quantities by following a volume element moving through the cylindrical discharge tube. This is possible since the flow rate allows to pinpoint the axial movement of the volume through the tube as a function of time. The considered volume, which is always assumed to be radially homogeneous, thus moves at a linear velocity v (as depicted in figure 6):

$$v = \frac{Q_m}{\rho A} \qquad (8)$$

where Q_m is the mass flow rate, $A = \pi R^2$ is the tube cross section area and $\rho = \sum n_i M_i$ is the gas mass density. n_i is the number density of species i and M_i is the mass of species i, while R is the tube radius.

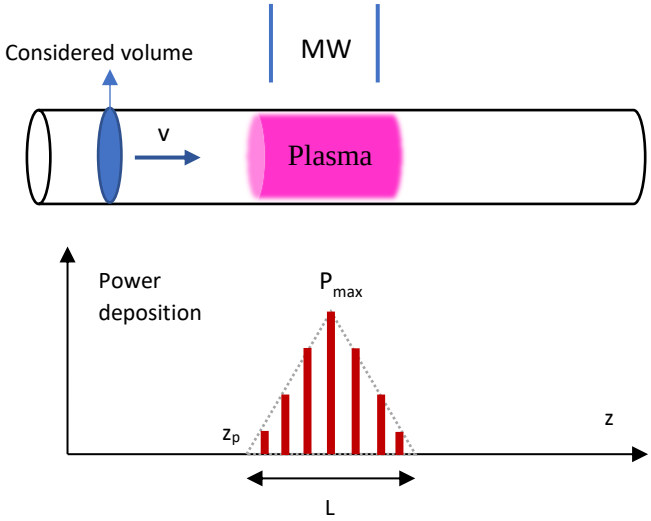

Figure 6: Schematic overview of setup and power deposition profile used in the 0D model.

By converting the time dependence of the 0D model into an axial dependence throughout the discharge tube, it is possible to express the power deposition as a function of z, the axial coordinate (see figure 6). For continuous power deposition, the profile of the power deposition is considered to be triangular, given by:

$$Q_{MW}(z) = \begin{cases} \left(1 - \left|\frac{z-\left(\frac{L}{2}\right)}{\frac{L}{2}}\right|\right) P_{max} & if\ z_p \leq z \leq z_p + L \\ 0 & otherwise \end{cases} \quad (9)$$

in which L is the plasma length, z_p is the axial coordinate at which the plasma starts and P_{max} is the maximum power deposition density (see figure 6). In a pulsed plasma, however, this triangular power deposition profile, which is depicted as a dotted line in figure 6, is only applied at certain points in time, depending on the frequency and the length of the pulses. The effective power deposition in the plasma is thus depicted as the red pulses in figure 6. From the applied power, the power density P is obtained through:

$$P = \frac{Q_{MW}}{V} \quad (10)$$

with V the (cylindrical) plasma volume. The power density is used to calculate the reduced electric field, i.e., the very important plasma parameter that is responsible for accelerating the electrons:

$$\frac{E}{n} = \frac{\sqrt{P/\sigma}}{n} \quad (11)$$

in which n is the plasma density and σ is the plasma conductivity, which is estimated using a E/n value of the previous calculation iteration.

As we are particularly interested in the temperature evolution in the plasma, the gas temperature T_{gas} is calculated self-consistently at all times by:

$$N\frac{\gamma k_B}{\gamma-1}\frac{dT_{gas}}{dt} = P_{el} - \sum_j R_j \Delta H_j - \frac{8\lambda}{R^2}\left(T_g - T_w\right) \quad (12)$$

where $\gamma = \frac{C_p}{C_v}$ is the specific heat ratio (the ratio of the isobaric and isochoric heat capacity), k_B is the Boltzmann constant, P_{el} is the power transferred from the electrons to the heavy particles through elastic collisions, ΔH_j is the enthalpy of reaction j, λ is the gas thermal conductivity and T_w is the wall temperature, assumed to be 300 K.

3.2 Chemistry set

As we are particularly interested in the vibrational ladder climbing mechanism of plasma-based nitrogen fixation, the chemistry of the model focusses excessively on the vibrational excitation and relaxation mechanisms in the plasma. For this reason, all 67 vibrational energy levels up to the dissociation limit of N_2 (9.765 eV) are included in the model, resulting in the list of plasma species presented in Table 1. The reactions between these species can be broken down in four different categories: (i) electron impact reactions, (ii) VT relaxation, (iii) VV relaxation and (iv) dissociation. A short overview of these four categories will be presented, while a full list is added to the Appendix.

(i) Electron impact reactions

This category includes electron impact ionization, dissociation, electron attachment, electron-ion recombination and electron impact excitation. The latter is especially important in this study as these electron impact reactions give rise to vibrationally excited species, triggering the vibrational ladder climbing. The rates of these reactions are calculated using the BOLSIG+ Boltzmann calculator, based on cross section data.[24]

Table 1: List of all plasma species included in the 0D model

Ground state species
N_2, N
Vibrationally excited species
N_2(V1-V67)
Electronically excited species
N_2 ($A^3\Sigma_u^+$), N_2 ($B^3\Pi_g$), N_2 ($W^3\Delta_u$), N_2 ($B'^3\Sigma_u$), N_2 ($C^3\ \Pi_u$), N_2 ($E^3\ \Sigma_g^+$), N_2 ($a'^1\Sigma_u^-$), N_2 ($a^1\ \Pi g$), N_2 ($a''^1\ \Sigma_g^+$), N_2 ($w^1\ \Delta_u$), N (2D), N (2P)
Ions
N_2^+

(ii) VT relaxation

These reactions are responsible for the energy exchange between vibrational and thermal energy. As a result of either gaining or losing energy in this transfer, the participant molecule goes up or down a vibrational level, respectively.

These rates are calculated using N_2 VT-rates from literature[26], scaled to all vibrational levels using the Schwartz–Slawsky–Herzfeld (SSH) theory:[27,28]

$$k_{n,n-1} = k_{1,0} Z_n \frac{F(\gamma_n)}{F(\gamma_1)} \tag{13}$$

where $k_{n,n-1}$ is the rate constant for VT relaxation N_2(Vn) → N_2(Vn-1) and $k_{1,0}$ is the basic rate constant for VT relaxation N_2(V1) → N_2, with n being the vibrational level of N_2.

The scaling factor Z_n is expressed as

$$Z_n = n\frac{1-x_e}{1-n_e} \tag{14}$$

where x_e is the anharmonicity of the energy levels of N_2. The function F is given by

$$F(\gamma) = \frac{1}{2}\left[3 - exp\left(-\frac{2}{3}\gamma\right)\right] exp\left(-\frac{2}{3}\gamma\right). \tag{15}$$

Finally, the parameter γ_n which is a measure of the adiabaticity of the reaction, is calculated as

$$\gamma_n = \frac{0.32\Delta E}{\alpha}\left(\frac{\mu}{T_{gas}}\right)^{1/2} \quad (16)$$

where $\Delta E = E_n - E_{n-1}$ is the change of vibrational energy in the collision, α (in Å^{-1}) is a parameter of the exponential repulsive potential between the colliding species, μ is their reduced mass and T_{gas} is their translational temperature.

(iii) VV relaxation

These reactions exchange vibrational energy between two molecules in which the molecule gaining vibrational energy is excited to a higher vibrational mode and the molecule losing energy to a lower vibrational mode. These energy exchanges are responsible for vibrational ladder climbing. These rates are calculated using N_2 VV rates from literature[26], again scaled to all vibrational levels using the SSH theory:

$$k_{n,n-1}^{m-1,m} = k_{1,0}^{0,1} Z_n Z_m \frac{F(\gamma_{nm})}{F(\gamma_{11})} \quad (17)$$

which is calculated analogously to the VT rate scaling, but now for two transitions in which one molecule lowers its vibrational state (n)→(n-1) and the other raises its vibrational state (m-1)→(m).

(iv) Dissociation

These reactions are ultimately the goal of N_2 fixation, breaking the triple bond of N_2 forming two N atoms. As the vibrational energy of excited molecules can help overcome the reaction energy barrier of the dissociation reaction, the reaction rate coefficient of the dissociation increases if the reacting N_2 molecule is excited to a higher vibrational energy level. This is taken into account by using the Fridman-Macharet dissociation model:[8]

$$k = A.exp\left(\frac{-E_a + \alpha E_v}{k_b T_{gas}}\right) \quad (18)$$

which uses a standard Arrhenius expression with E_a the activation energy of the dissociation reaction and k_b the Boltzmann constant, but adds an extra factor αE_v. This factor involves the vibrational energy E_v of the molecules into the equation, as well as a factor α (between 0 and 1) that scales E_v for the case when the activation energy is higher than the dissociation limit.

3.3 Experimental data as input for the model

To be able to compare the experimental and modelling results, both should be run for the same plasma parameters. As a result, the calculation parameters are chosen to match the experimental pressure of 25 mbar and the flow rate of 4 slm. However, the power density is not as easily defined as the pressure or the flow rate, since it depends on the power profile of the pulse, as well as the shape of the plasma. In order to achieve a power density input for the model, these two aspects, i.e., the experimental power deposition and the plasma shape, are investigated.

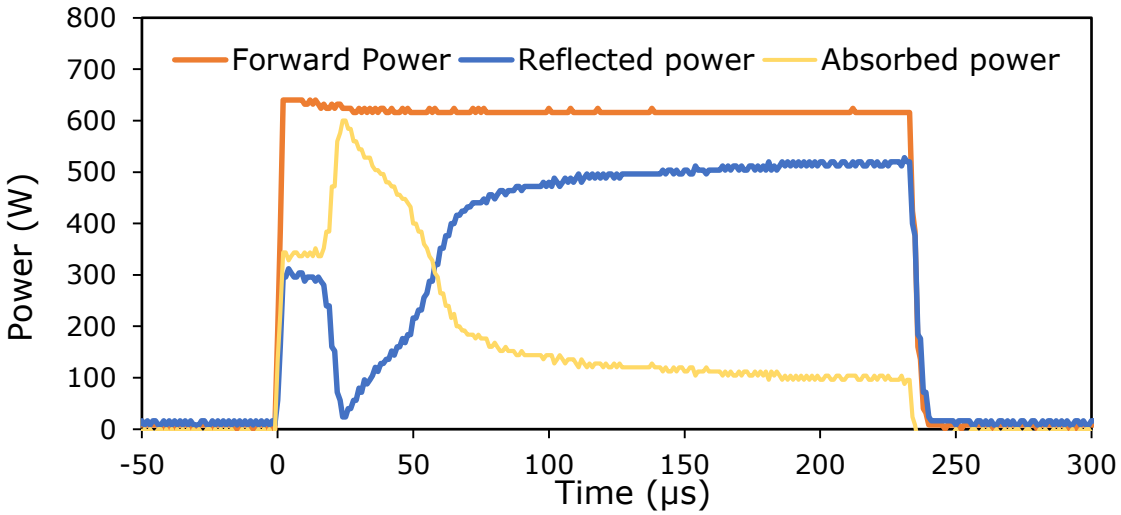

Figure 7: Experimental power deposition profile through a 233 µs pulse, showing the forward power, reflected power and absorbed power.

During each experiment, the power deposition throughout the pulse is monitored by measuring the reflected MW power through a diode in the wave guide. Subtracting this reflected power from the 600 W pulse signal operated by the signal generator, yields the absorbed power in the pulse. This subtraction is depicted in figure 7, delivering the input for the power deposition for the model.

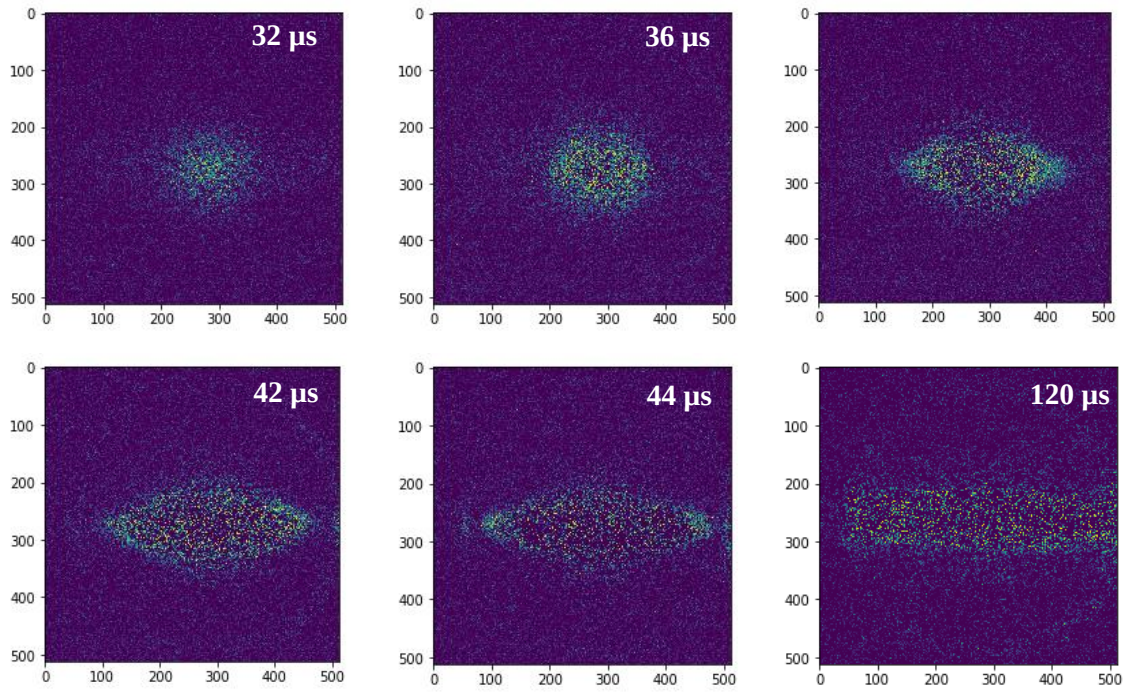

Figure 8: Evolution of the axial plasma shape in a 233 µs pulse. The pictures are taken 32, 36, 38, 42, 44 and 120 µs after igniting the plasma, respectively.

The shape of the plasma is also investigated in a separate imaging experiment. Instead of filtering out the light and guiding it through a spectrometer, the plasma is directly imaged by the iCCD camera through an opening in the waveguide. These resulting images, showing the ignition and the development of the plasma through a 233 µs pulse, are depicted in figure 8. This series of images gives a good estimation of the evolution of the plasma shape throughout the pulse and can thus be used to describe the power density. Indeed, the images reveal that in the first stages of the pulse, the plasma volume is very small, concentrating all deposited power in a very small area. Taking into account the evolution of the plasma volume (approximated by a cylinder, with the radius and length measured from the picture scale), the power density evolution through the pulse is calculated using equation 10 and is depicted in figure 9. This figure clearly shows that the power density is very high in the first few microseconds of the pulse, due to the small initial plasma volume, and almost constant in the rest of the pulse. The small peak around 25 µs is a result of the maximum absorbed power in that time frame in figure 7. This observed evolution of the power density through time in figure 9 will be taken as an input for the pulse shape in the model, but only for the pulses that occur when the considered gas element is in the centre of the plasma. Only there, the considered gas is in the initial small plasma volume when a pulse begins and thus only then the gas experiences the initially high

power density. For pulses occurring out of this initial volume, the first part of the power density evolution does not apply and the power density is approximated solely by the constant part, depicted in the inset figure of figure 9. Describing the power density differently in the centre of the plasma can be seen as a correction for the 0D model not taking into account that the plasma ignites from a small volume in the beginning of each pulse.

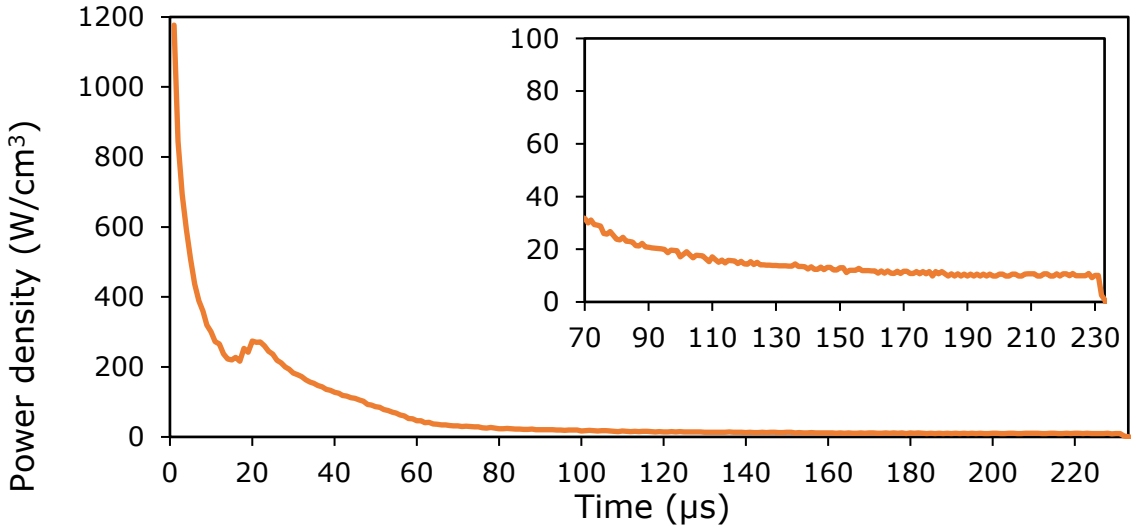

Figure 9: Evolution of the power density through a 233 µs pulse, considering the power deposition profile in figure 7 and the shape of the plasma in figure 8. The inset figure shows the part of the power density being considered constant in the model.

4. Results and discussion

Three different kinds of experiments and corresponding model calculations will be conducted to investigate the behaviour of a pulsed plasma regime.

- First, the temperature evolution of one single pulse of 233 µs will be examined.
- Subsequently, a large number of pulses will be applied, examining the temperature evolution at a pulse frequency of 1000 Hz, 2000 Hz, 5000 Hz and 7000 Hz using a constant pulse width of 50 µs.
- Finally, the effect of different pulse widths will be examined, using 10 µs, 50 µs, 200µs and 400 µs pulses, while the pulse frequency is kept at 1000 Hz.

All the conducted measurements and calculations are performed using a pressure of 25 mbar and a N_2 flow rate of 4 slm.

4.1 One pulse condition

To obtain an initial understanding of the vibrational excitation in pulsed MW plasmas, the excitation process is first studied when only one single pulse is applied to the gas. This will provide fundamental information about the non-equilibrium between the vibrational and gas temperature that exists in pulsed plasmas. This one pulse plasma is experimentally achieved by pulsing at such a low frequency (30 Hz) that no gas molecule will ever see more than one pulse when passing through the plasma tube. This is combined with a high flow rate of 4 slm, constantly providing new gas to the plasma. The low frequency and high flow rate will thus make sure that pristine, not heated, undissociated gas is always present in the tube when a MW pulse arrives. The duration of the pulse is chosen to be 233 µs, while the pressure is 25 mbar. By using Raman spectroscopy at different time frames in the 233 µs pulse, the profile of the vibrational and gas temperature through the pulse is captured. This temperature profile, shown in figure 10a, as well as the Raman spectra leading to these measured temperatures, will be discussed.

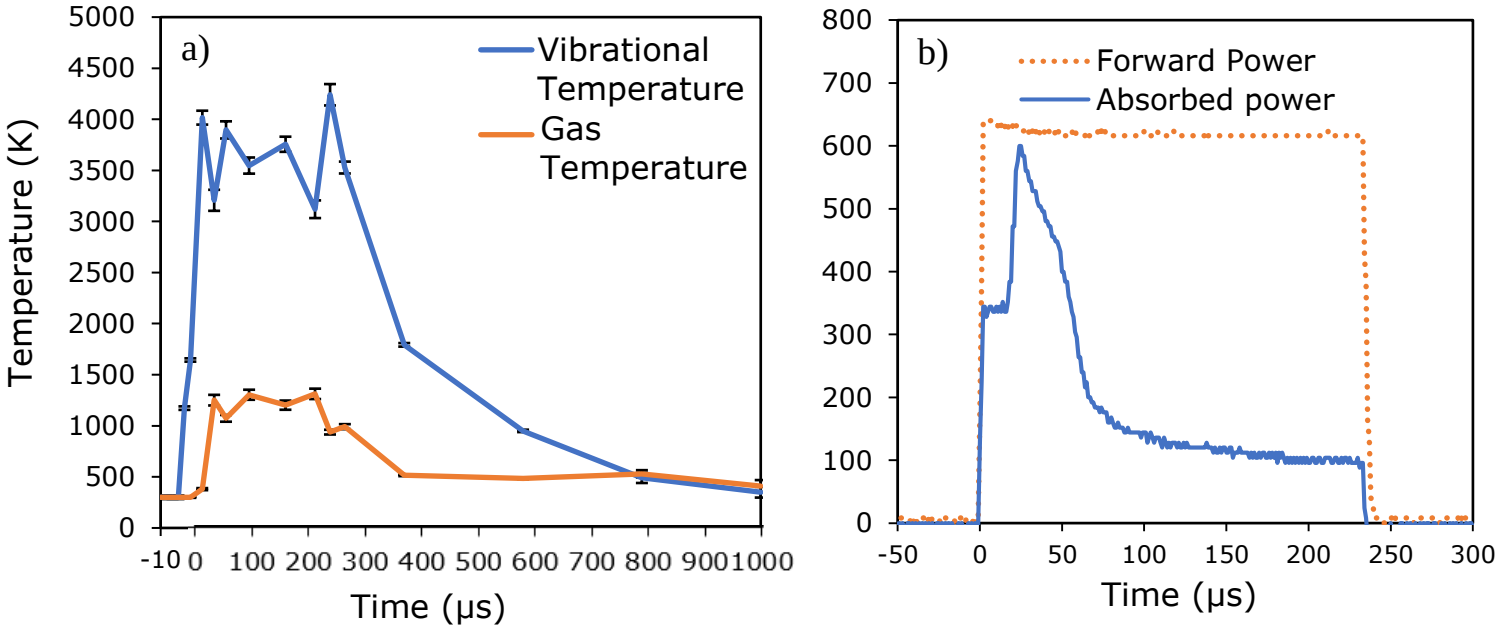

Figure 10: Evolution of the vibrational and gas temperature in the centre of the plasma (a), and of the measured power deposition (b), during one single 233 µs pulse and tis afterglow.

Right before the start of the pulse at -10 µs in figure 10a, no MW radiation has been applied yet. The vibrational temperature as well as the gas temperature are in thermal equilibrium, both at room temperature. This data point supports the previously made statement that the gas is unheated when the power pulse is applied. The Raman spectrum at this time frame, shown in figure 11, clearly shows that only ground state N_2 molecules are significantly excited by the laser. This means that no significant overpopulation of vibrational levels is present at this time.

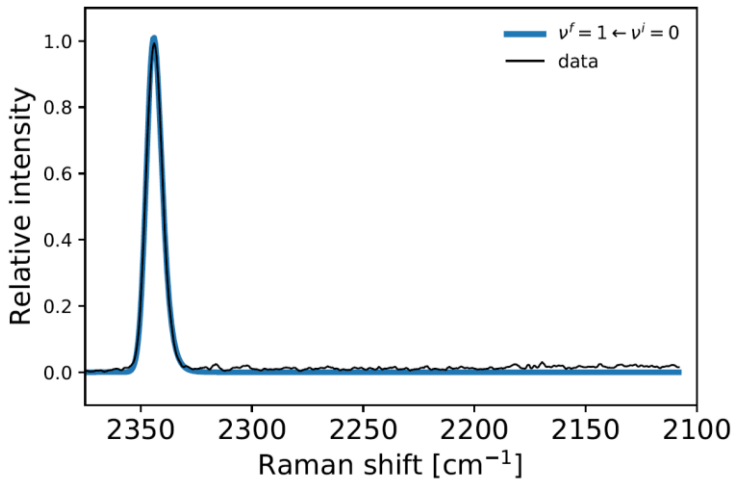

Figure 11: Raman spectrum acquired 10 µs before the start of the pulse. The blue line shows the fitted Raman transition

This same situation still persists at the very first time frames of the pulse (0 – 20 µs), as the plasma has yet to be fully formed, as indicated in figure 8 above.

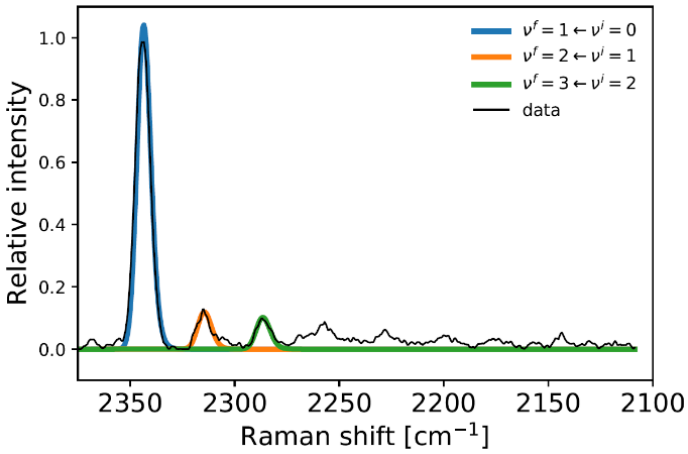

Figure 12: Raman spectrum acquired 30 µs after the start of the pulse. The coloured lines show the fitted Raman transitions.

At 30 µs, additional peaks clearly become distinctive in the Raman spectrum, shown in figure 12, indicating that the vibrational excitation has begun. The plasma ignition has progressed enough to start populating the first vibrational levels, slowly increasing the vibrational temperature. This time frame corresponds to the maximum in absorbed power in figure 10b, at which point all the forward power is fully absorbed. This max absorption of MW energy by the present electrons pushes the plasma to the point at which vibrational excitation is visible. At the same time the gas temperature still resides at 300 K, which demonstrates that nearly all power is put into the electrons and not into gas heating. This clearly shows the thermal non-equilibrium between electrons and gas particles present in a MW plasma.

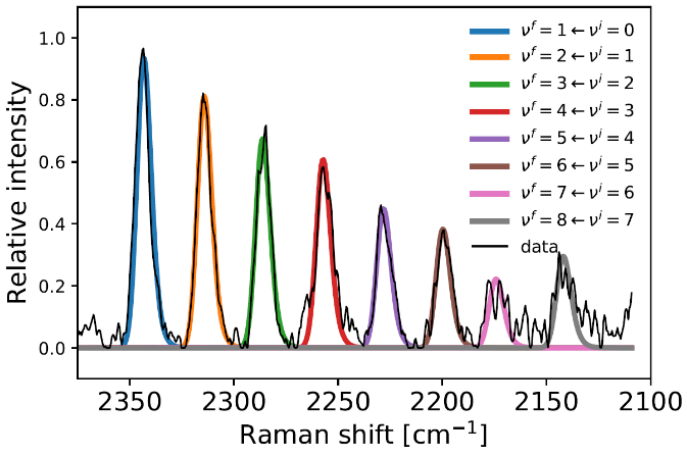

Figure 13: Raman spectrum acquired 60 µs after the start of the pulse. The coloured lines show the fitted Raman transitions.

From the 30 µs time frame on, the vibrational temperature keeps rising as more vibrational excitation reactions occur. At this point, shown in figure 10b, less power is absorbed by the plasma, as the electron density medium becomes less penetrable for MW radiation.[29] The rise of the vibrational temperature reaches its peak at 60 µs. At this time, vibrational excitation has achieved highly populated vibrational levels, which is clearly shown by the distinctive peaks of high intensity in the Raman spectrum in figure 13. At 60 µs a vibrational temperature above 4000 K is achieved, while the gas temperature is still around 300 K, displaying a clear, highly promising, non-equilibrium situation. However, from this point on, the gas itself starts to heat, which is visible in figure 10a by the rising gas temperature. This means that processes like VT relaxation or recombination of atomic N start to become important, heating the gas and slowly dismantling this highly favoured non-equilibrium.

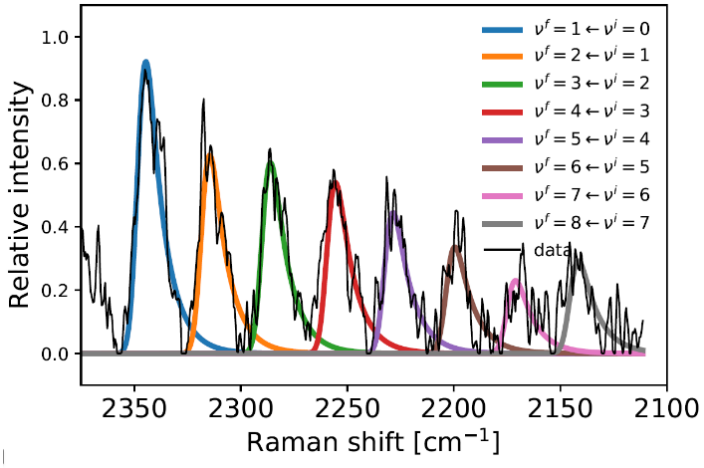

Figure 14: Raman spectrum acquired 200 µs after the start of the pulse. The coloured lines show the fitted Raman transitions.

With heating processes coming into action past 60 µs, the bands in the Raman spectrum broaden, as is visible in the Raman spectrum at 200 µs, shown in figure 14. At this point, which is near the end of the pulse, the gas temperature has risen to roughly 1200 K, resulting in more rotational levels being populated, broadening the vibrational bands in the spectrum. Besides the broadening of the bands, the high gas temperature is also responsible for a significant decrease in signal-to-noise ratio. As the pressure remains constant at 25 mbar, the high temperature drastically decreases the gas density, leaving less molecules to provide a Raman signal.

Although the gas temperature has risen to 1200 K, the vibrational temperature remains between 3500 and 4000 K. Thus, the energy applied in the last 140 µs of the pulse does not further raise the vibrational temperature. Instead it gives rise to either VV relaxation, which pumps the invested energy up the vibrational ladder where it is used for dissociation, or to heating

processes like VT relaxation, which raise the gas temperature to 1200 K. The fact that the VT relaxation starts later in the pulse represents the difference in time scale at which VV relaxation, VT relaxation and electron impact vibrational excitation occur. As pointed out by Capitelli et al.[30], the typical relaxation time of these three major reactions can be calculated using their reaction rates constants and the species densities:

$$\begin{aligned} \tau_{e-V} &= \left(n_e k_{e-V}^{1,0}\right)^{-1} = 0.49\ s \\ \tau_{VV} &= \left(N_{N_2} k_{0,1}^{1,0}\right)^{-1} = 180\ \mu s \\ \tau_{V\,T} &= \left(N_{N_2} k^{1,0}\right)^{-1} = 9860\ s \end{aligned} \tag{19}$$

These relaxation times represent the time in which complete relaxation occurs through electron impact excitation (τ_{e-V}), VV relaxation (τ_{VV}) and VT relaxation (τ_{VT}) using the density of ground state nitrogen (N_{N_2}), the electron density (n_e) and the respective reaction rate coefficients for ground state nitrogen at 300 K. The values of the relaxation times clearly show that VT relaxation occurs on a much longer time scale than VV relaxation and electron impact vibrational excitation. Especially the time scale difference of 10^9 between VV and VT relaxation is notable. This explains why the increase in gas temperature lags behind the fast increase in vibrational temperature.

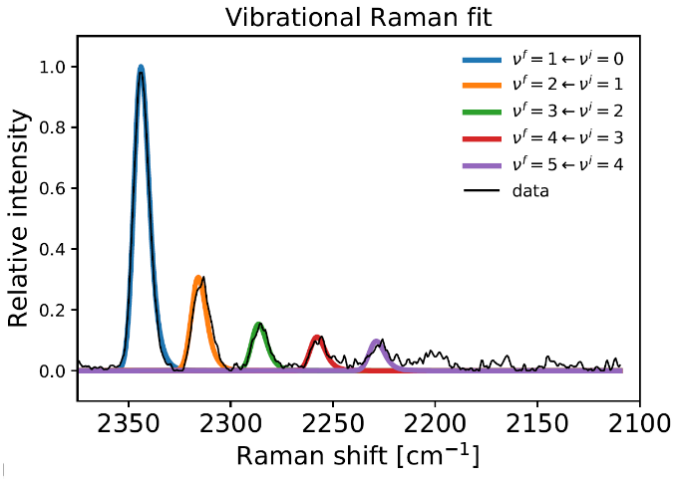

Figure 15: Raman spectrum acquired 400 µs after the start of the pulse. The coloured lines show the fitted Raman transitions.

After the finalisation of the pulse at 233 µs, no more power is applied, removing any excitation mechanisms. During this time, the observed section of the plasma tube cools down both rotationally and vibrationally. The Raman spectrum at 400 µs, depicted in figure 15, clearly shows that the vibrational levels are depopulating, since the different peaks are losing intensity. As shown in figure 10a, over a period of about 550 µs, both the vibrational and gas temperature cool down to 300 K, reaching thermal equilibrium around 800 µs after the start of the pulse. In

this process, the gas temperature cools down rather fast, which indicates heat is dissipating away from the centre of the tube.

The temperature evolution of this one pulse experiment provides an interesting view of the time scales of the fundamental mechanisms occurring in one single pulse. In these conditions a clear non-equilibrium is achieved after 60 µs,but is partially compensated by the rising gas temperature shortly after. By the end of the pulse, a vibrational temperature around 4000 K and a gas temperature around 1200 K are reached, which both cool down to 300 K around 550 µs after termination of the pulse. A more in-depth insight of these observed mechanisms can be acquired using the 0D model. The temperature profile through the 233 µs pulse and its afterglow, calculated using the model, is depicted in figure 16.

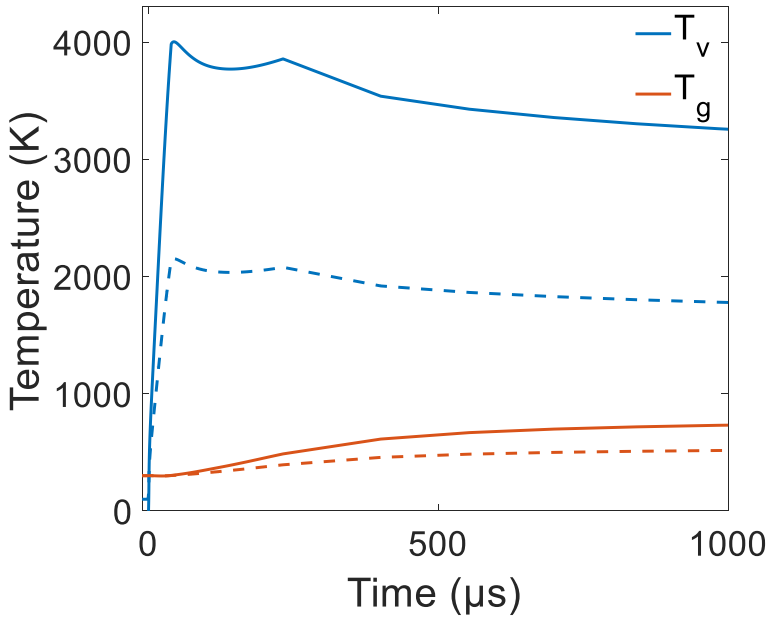

Figure 16: Calculated vibrational temperature and gas temperature through one single 233 µs pulse and its afterglow. The dashed lines represent the temperatures averaged over the whole plasma, as calculated by the 0D model. The full lines represent the temperatures in the centre of the plasma, calculated through equation 20.

It should be mentioned that the calculated temperatures cannot be compared straight out with the experimental data. The calculated temperatures represent a radially averaged temperature, which is logical with a 0D model, while the experimental data show the temperature in the centre. If assumed that the radial temperature profile is parabolic, the radially averaged temperature in the centre (T_{avg}) can be expressed as:

$$T_{avg} = \frac{\int_0^{2\pi}\int_0^R \left(\frac{T_w - T_0}{R^2} r^2 + T_0\right) r\,dr\,d\phi}{\pi R^2} \qquad (20)$$

in which T_w is the temperature of the wall, assumed to be 300 K, T_0 the temperature in the centre of the tube, r the radial coordinate in the tube, R the radius of the tube and ϕ the radial angle in the tube. Solving this equation yields $T_0 = 2\,T_{avg}$ -300.

This factor should thus be taken into account when comparing the averaged uniform temperature of the 0D model and the temperature in the centre which is measured in the experiments. In figure 16, both the averaged temperature and the temperature in the centre calculated through equation 20 are displayed by the dashed and full lines respectively. From now on, this factor will always be implemented for comparing gas temperatures. Furthermore, as the radial density of excited nitrogen is observed to be parabolic when it is excited in the centre of a tube[31], this factor will also be implemented for comparing vibrational temperatures.

A comparison between figure 16 and figure 10a demonstrates the accuracy at which the model predicts the vibrational temperature. As observed in the experimental temperature profile, the calculations show that a vibrational temperature of 4000 K is reached almost instantly when power is applied, due to the short time scale at which vibrational excitation occurs. While the vibrational temperature is very accurately predicted, the calculated gas temperature is clearly underrated in comparison to the experiment. The model predicts a gas temperature around 600 K in the pulse, while the experiment indicates a temperature of 1200 K. However, in both cases, the same trend through the pulse is observed: The gas temperature rises much more slowly, as heating reactions occur on longer time scales. While the behaviour of the gas temperature and vibrational temperature inside the pulse are well predicted, a clear difference between figure 16 and 10a is observed upon termination of the pulse. The model predicts both the gas temperature and vibrational temperature to relax more slowly than shown in figure 10. This supports the earlier hypothesis that dissipation processes, which are not taken into account in a 0D model, are responsible for a fast decline in temperature in the centre of the tube, rather than relaxation processes.

An explanation for the observed temperature profiles in figure 10a and 16 is provided by the 0D model, through calculating the reaction rates of the three most important excitation and relaxation processes in the plasma: electron impact vibrational excitation, VV relaxation and VT relaxation. For each of the three reactions, the reaction rates from all 67 vibrational levels were summed and multiplied with the energy difference of the transition. The multiplication with the energy difference is taken into account to make figure 17 a representation of how the three reactions distribute the applied energy over the whole vibrational ladder. In this figure a

negative reaction rate indicates that the reaction is bringing energy down the vibrational ladder, by inducing a net depopulation of the vibrational levels, while positive reaction rates indicate that the reaction pumps energy up the vibrational levels, by inducing a net population. The relative ratio of the three major plasma processes in figure 17 provides an explanation for the current situation. The figure clearly shows how electron impact vibrational excitation and VV relaxation rates are very high in this one pulse regime, inducing high vibrational temperatures instantly as the pulse begins. The VT relaxation rates, however, are low through the whole pulse, explaining why slow gas heating is observed in figure 10a and 16. These rates confirm the prediction made by the relaxation times in equation 19, which indicated that VT relaxation occurs on a much slower time-scale than VV relaxation and electron impact excitation processes. The pulsed situation represented here takes advantage of these different time scales: terminating the power supply frequently, as done in this pulsed plasma, inhibits the rates of the slow VT relaxation process to grow to high values, while fast reactions, like electron impact vibrational excitation and VV relaxation, have no problem to occur on this short time scale.

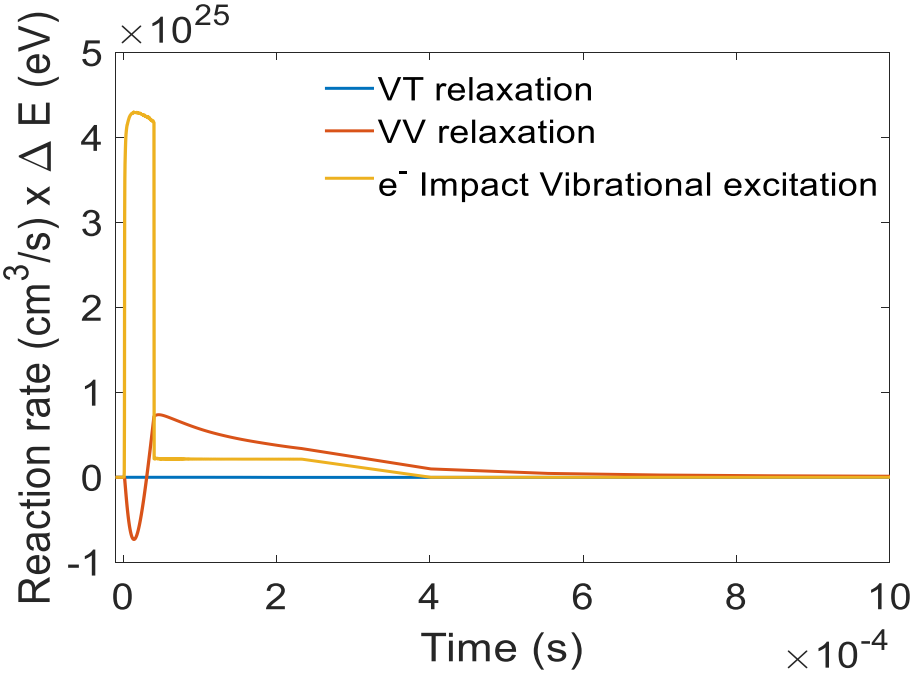

Figure 17: Reaction rate profiles of electron impact vibrational excitation, VV relaxation and VT relaxation throughout one single 233 µs pulse of the MW plasma and its afterglow, The reaction rates from all 67 vibrational levels were summed and multiplied with the energy difference of the transition (see text).

Particular in this regime are the negative VV rates in the pulse, shown by figure 17. During the pulses, electron impact vibrational excitation is promoted so well, causing such an excessive vibrational population, that it is depopulated by VV relaxation (i.e. a ladder down climbing).

After 50 µs, the VV rates are positive again, pumping molecules back up the vibrational ladder. This observation shows that during the pulses, electron impact excitation is the most important vibrational excitation mechanism to populate vibrational levels over the whole vibrational ladder. The importance of electron impact excitation in every level of the vibrational ladder was already observed by Capitelli et al.[30] for plasmas in the µbar pressure range, in which the low pressure inhibited relaxation processes. The pulsed mbar plasma presented here appears to demonstrate the same importance of electron impact vibrational excitation.

The excessive population of vibrational levels by electron impact vibrational excitation, as well as the limited contribution of VT relaxation, is also represented in the vibrational distribution function (VDF) of the one pulse regime. Figure 18 shows the VDF 10µs, 100 µs, 233 µs and 1000 µs after the start of the pulse. As the pulse ends after 233 µs, the VDF at 1000 µs shows the result in the afterglow of the plasma. A critical note has to be made that the model was not yet able to fully predict a Boltzmann distribution for the populations before the plasma, so this needs to be checked further, but it was not possible anymore within the time frame of the master thesis. However, useful information can still be acquired about the general trends of vibrational excitation that occur in the plasma. In figure 18 it is clear that progressing through the pulse, the higher vibrational levels get more and more populated. By the end of the pulse, the population of vibrational levels has reached a stationary distribution, in which all higher vibrational levels are almost equally populated. This gives the VDF a characteristic shape of a plateau that ultimately declines towards the highest vibrational levels. Molecules excited to these highest vibrational levels barely experience an energy barrier to overcome the dissociation reaction, which is why they are almost immediately dissociated. The characteristic shape of a plateau thus indicates that at this point, molecules are constantly pumped towards the higher energy levels to eventually dissociate. This is a beneficial situation, as the purpose of this research is to dissociate N_2 through this vibrational ladder climbing. Furthermore, the VDF at 1000 µs shows that the overpopulation of the higher vibrational levels barely relaxes in the afterglow, indicating that even in the afterglow, N_2 is still dissociating.

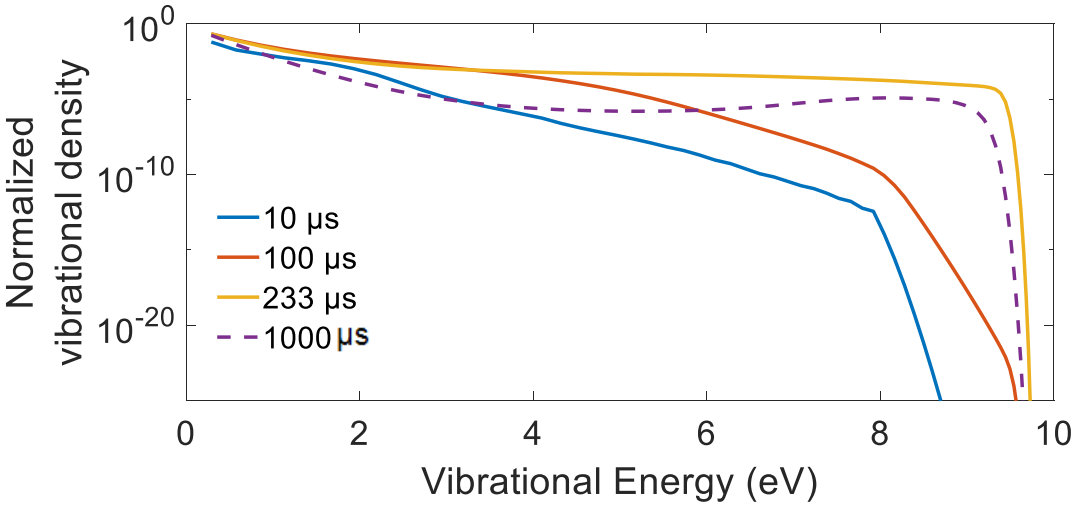

Figure 18: VDF at three different time frames during a 233 µs pulse (full lines) and one time frame in the afterglow (dashed line)

While a lot of fundamental information can be extracted from these one pulse experiments, their application potential for industrial N_2 fixation is unlikely. Indeed, pulsing the power at 30 Hz with a gas flow rate of 4 slm allows a large portion of the gas to pass through the reactor in the pulse off-time, missing out on any vibrational excitation. Furthermore, the gas that experiences this one pulse, has a very short residence time in the plasma. Although no conversions to atomic nitrogen or energy efficiencies were measured during these experiments, it can be stated that this one pulse situation is hardly efficient for real N_2 fixation. Therefore, in this thesis, next to this one pulse experiment, regimes of higher frequencies are also investigated. The following cases will thus elucidate to which degree the fundamentals of the one pulse plasma extend to more realistic, higher frequency situations. Again, the focus will be put on the vibrational temperature and gas temperature and how a non-equilibrium is formed in the plasma. Using both experimental and computational data, the distinctive features and advantages of a 1000 Hz, 2000 Hz, 5000 Hz and 7000 Hz pulsed MW plasma will be investigated.

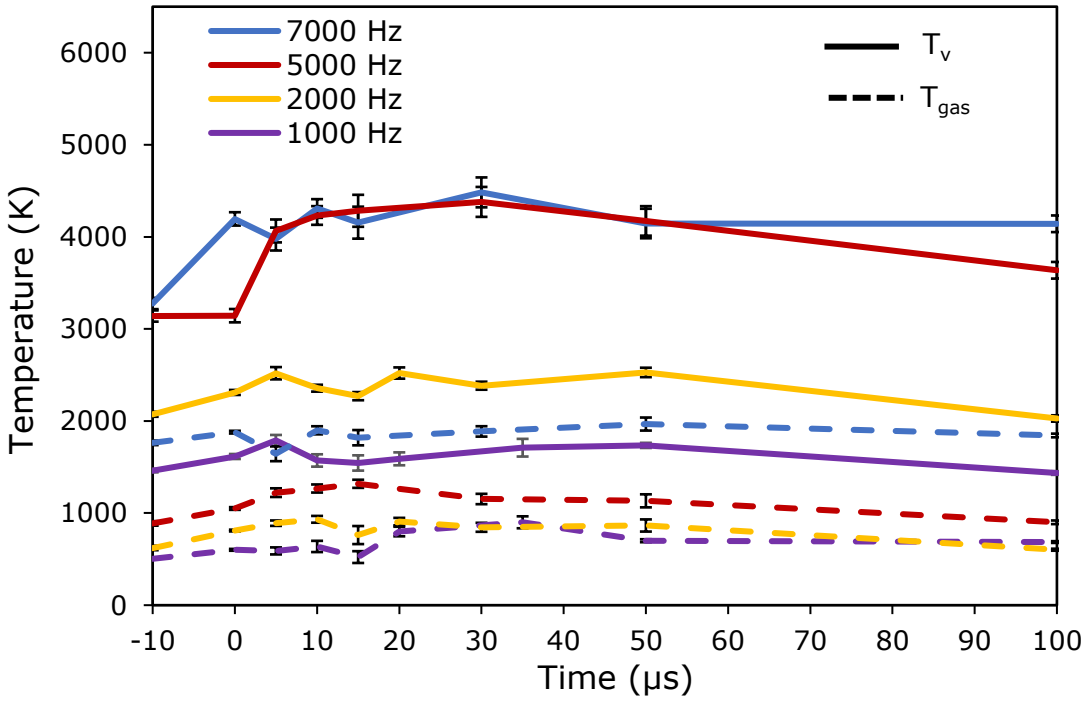

Figure 19: Vibrational temperature (full lines) and gas temperature (dashed lines) profile through a single pulse of a 1000 Hz, 2000 Hz, 5000 Hz and 7000 Hz pulsed MW plasma, with a pulse width of 50 µs..

Figure 19 shows the temperature profiles, obtained from the Raman experiments, for pulse frequencies of 1000 Hz, 2000 Hz, 5000 Hz and 7000 Hz, and a 50 µs pulse width. The dashed lines represent the gas temperatures, while the full lines represent the vibrational temperatures throughout a single pulse and its afterglow. An exemplary spectrum from which temperature data is extracted, is found in the Appendix. For the analysis of figure 19, it has to be pointed out that each presented temperature profile is an averaged profile for all the pulses that the gas experiences when flowing through the plasma. The Raman scattered light is captured over the whole length of the plasma, meaning that during the recording of each spectrum, light is scattered on molecules that already saw 10 pulses and are near the end of the tube, as well as molecules that only saw one pulse, in the beginning of the tube. The temperature profile provides thus an averaged snapshot of the whole state of the plasma in that specific time frame. However, while the data is averaged over the length of the tube, it always represents the temperature in the radial centre of the tube, where the laser is focussed.

While all temperature profiles in Figure 19 show a very clear non-equilibrium between vibrational and gas temperature it is clear that increasing the pulse repetition frequency has a direct impact on the vibrational and gas temperature in the plasma. As more pulses are applied in the same period of time, i.e. of a higher frequency, more power is put into the plasma, which leads to more vibrational excitation and thus a higher vibrational temperature. Therefore, the vibrational temperature rises upon reaching higher pulse frequencies. However, vibrational excitation is not the only reaction that gains significance by increasing the pulse frequency. The gas temperature also raises notably upon rising frequency, indicating that reactions like atomic N recombination or VT relaxation also gain significance. The latter might explain why the measured vibrational temperature in the 7000 Hz plasma is not significantly higher than the vibrational temperature in the 5000 Hz plasma, while the gas temperature has strongly increased.

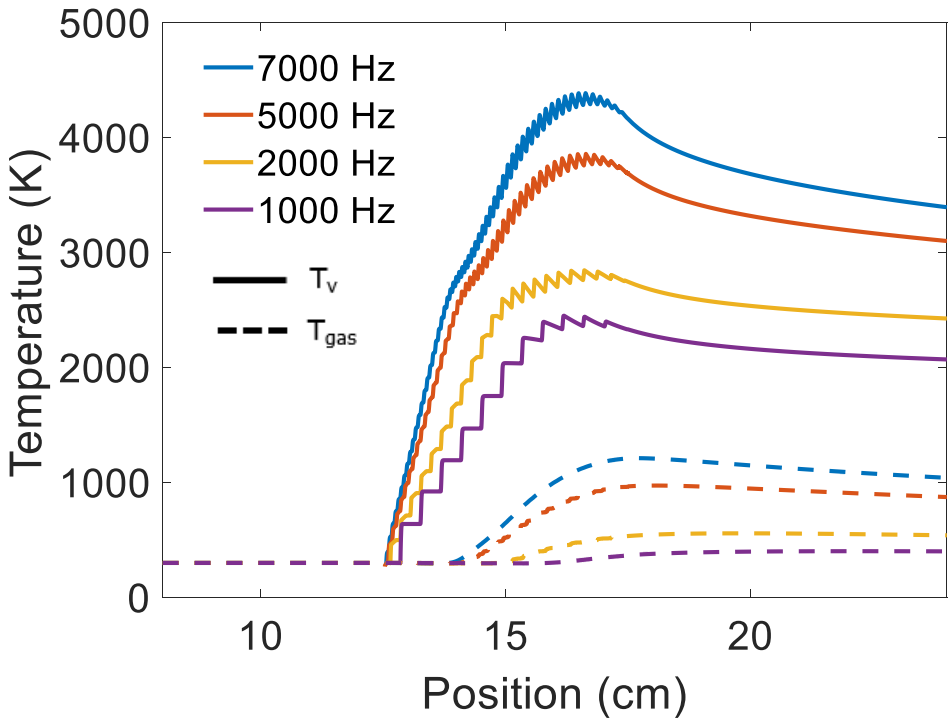

Figure 20: Calculated vibrational and gas temperature profile through a 1000 Hz, 2000 Hz, 5000 Hz and 7000 Hz pulsed MW plasma, all with a pulse width of 50 µs. The full lines represent the vibrational temperatures, the dotted lines the gas temperature.

The temperature profiles calculated with the 0D model for the different frequencies are plotted in figure 20, as a function of position in the plasma tube, after the gas experiences various power deposition pulses. These profiles present the same trend as observed in the experiments, i.e., a higher pulse frequency yields a higher vibrational and gas temperature. In addition, these

profiles display another trend in the evolution of the temperature through the plasma. At higher frequencies, after reaching the maximum value, the vibrational temperature starts to decline. The fact that this decline is indeed more pronounced at higher frequencies, shows that the vibrational levels are getting depopulated faster by relaxation processes. The fast decline of vibrational temperature is also accompanied with an earlier rise in gas temperature, indicating that it is caused by VT relaxation. Just like the experimental temperature profiles, the calculated temperature evolution suggests that VT processes occur faster at higher frequencies.

To critically compare the experimental and calculated temperature profiles, the calculated profiles are presented in figure 21, the same way as the experimental data in figure 19, as one position averaged pulse profile. This is achieved by averaging out every pulse of figure 20 for each of the four pulse frequencies and allows an accurate comparison to be made of the vibrational and gas temperature achieved in the experiment and the calculations. This comparison is shown in figure 22, using the average temperature in the pulse profile as a comparative measure for each frequency. The comparison shows that the vibrational temperature is quite accurately predicted, which is highly favourable, since the focus of the model was on the vibrational mechanisms in the plasma. The gas temperature, however, is systematically underestimated. Especially the 7000 Hz frequency values are predicted too low, meaning that some heating mechanism in the plasma is not yet well described. However, the trend that the gas temperature rises with increasing frequency matches the experimental observations. Although it is not as pronounced as in the experiments, it indicates that the trends of the gas temperature can still be predicted by the model.

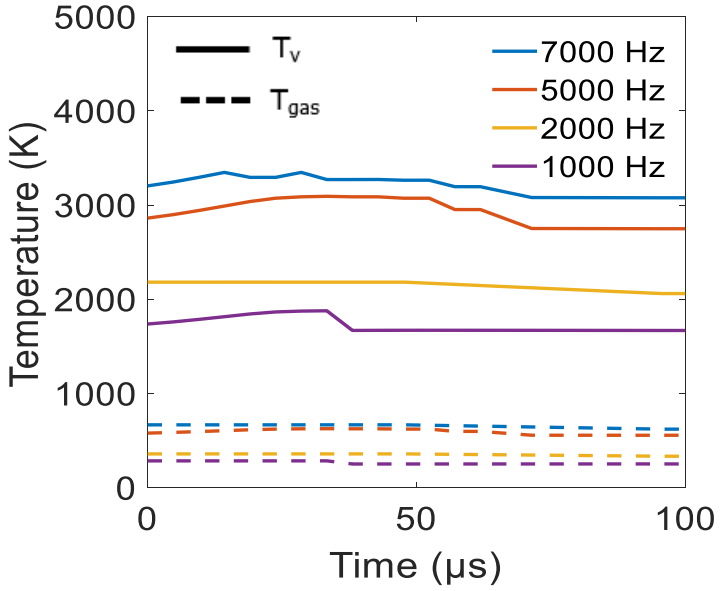

Figure 21: Calculated vibrational and gas temperature profile through a 1000 Hz, 2000 Hz, 5000 Hz and 7000 Hz pulsed MW plasma, averaged out over every pulse. The full lines represent the vibrational temperatures, the dotted lines the gas temperature.

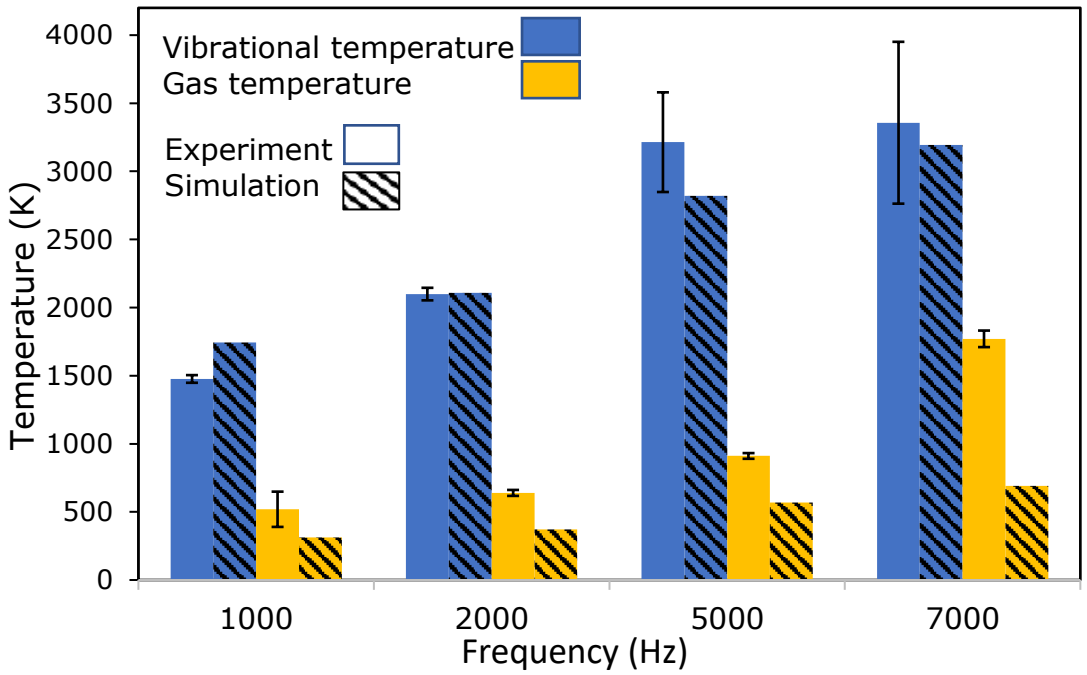

Figure 22: Measured and calculated averaged vibrational and gas temperatures in a pulsed MW plasma at four different frequencies.

Having validated the calculated temperature profiles, the model can be used to further explain the observations made in the experimental and calculated temperature profiles. These profiles indicated reaction mechanisms like VT relaxation increased in significance upon raising the pulse frequency. To clearly demonstrate the influence of the pulse frequency on the major reactions in the plasma, the reaction rates of electron impact vibrational excitation, VV relaxation and VT relaxation throughout the plasma are shown in figure 23, for both the 1000 Hz and the 7000 Hz pulse repetition frequency, respectively. Again, the reaction rates from all 67 vibrational levels were summed and multiplied with the energy difference of the transition (cf. above). A comparison between the reaction rate profile of the 1000 Hz and 7000 Hz regime indicates in the first place that in a higher pulse frequency electron impact vibrational excitation is much more significant. Figure 23 shows that the absolute values of the electron impact reaction rate in the 7000 Hz regime are the same as in the 1000 Hz regime, yet these values are reached seven times more often in the reaction rate profile at 7000 Hz than at 1000 Hz, resulting in seven times more vibrational excitation. The more significant vibrational excitation at higher pulse frequencies can also be observed in the evolution of the VDF, calculated for a 1000 Hz and 7000 Hz pulse regime in figure 24. The VDFs are plotted for different locations in the power density profile, indicating the development of the VDF through the pulsed regime. Like in the one pulse regime, both the VDFs of the 1000 Hz and 7000 Hz regime eventually reach

stationary state in which all the higher vibrational levels are overpopulated, resulting in the VDF having the characteristic shape of a plateau. However, due to the more frequently occurring vibrational excitation in the 7000 Hz regime, this stationary phase is reached much earlier in the plasma pulsed at 7000 Hz.

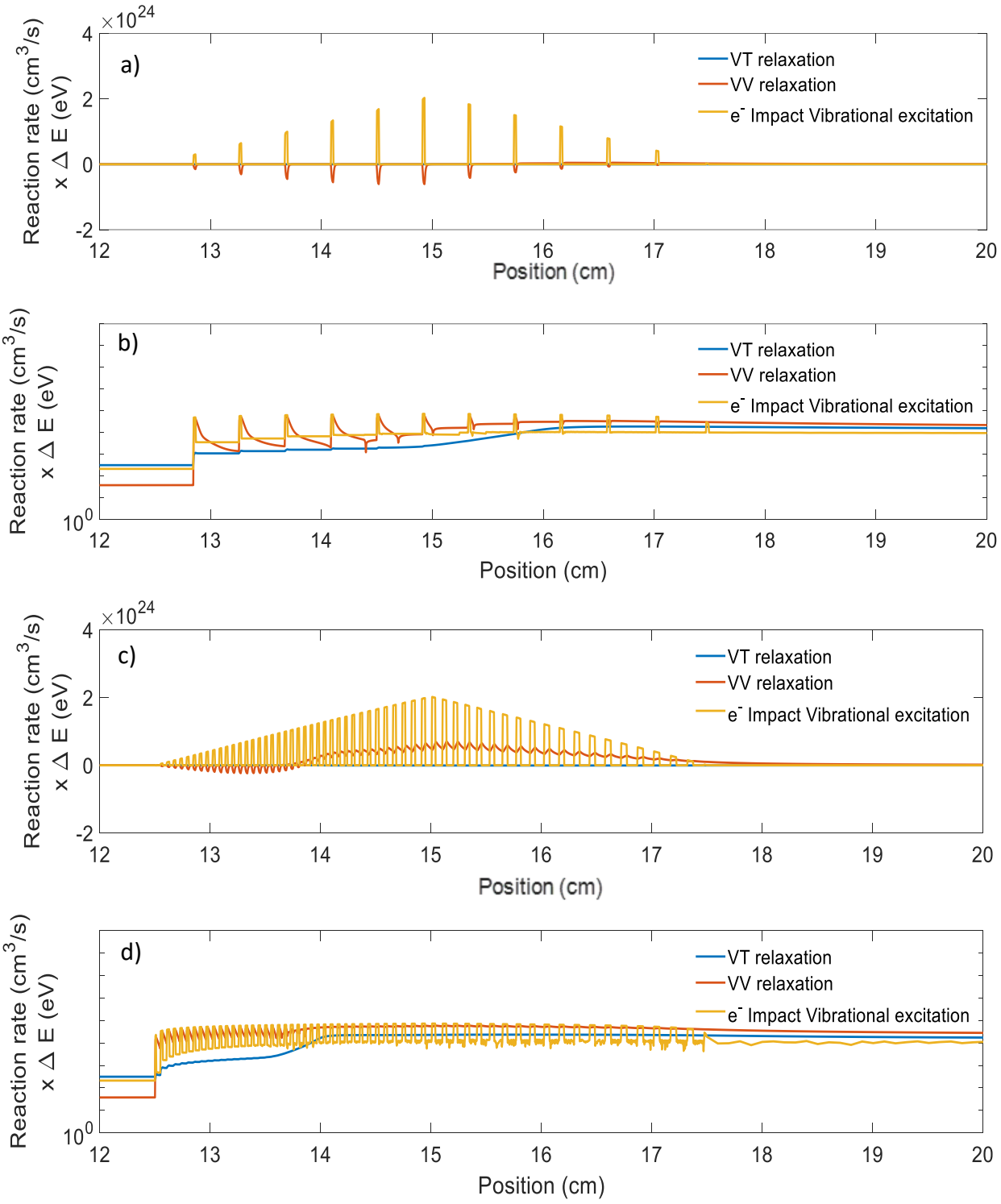

Figure 23 a: Reaction rate profiles of electron impact excitation, VV relaxation and VT relaxation throughout a 7000 Hz pulsed MW plasma, both linearly scaled and log scaled for a 1000 Hz (a and b) and 7000 Hz (c and d) regime. The reaction rates from all 67 vibrational levels were summed and multiplied with the energy difference of the transition, as before.

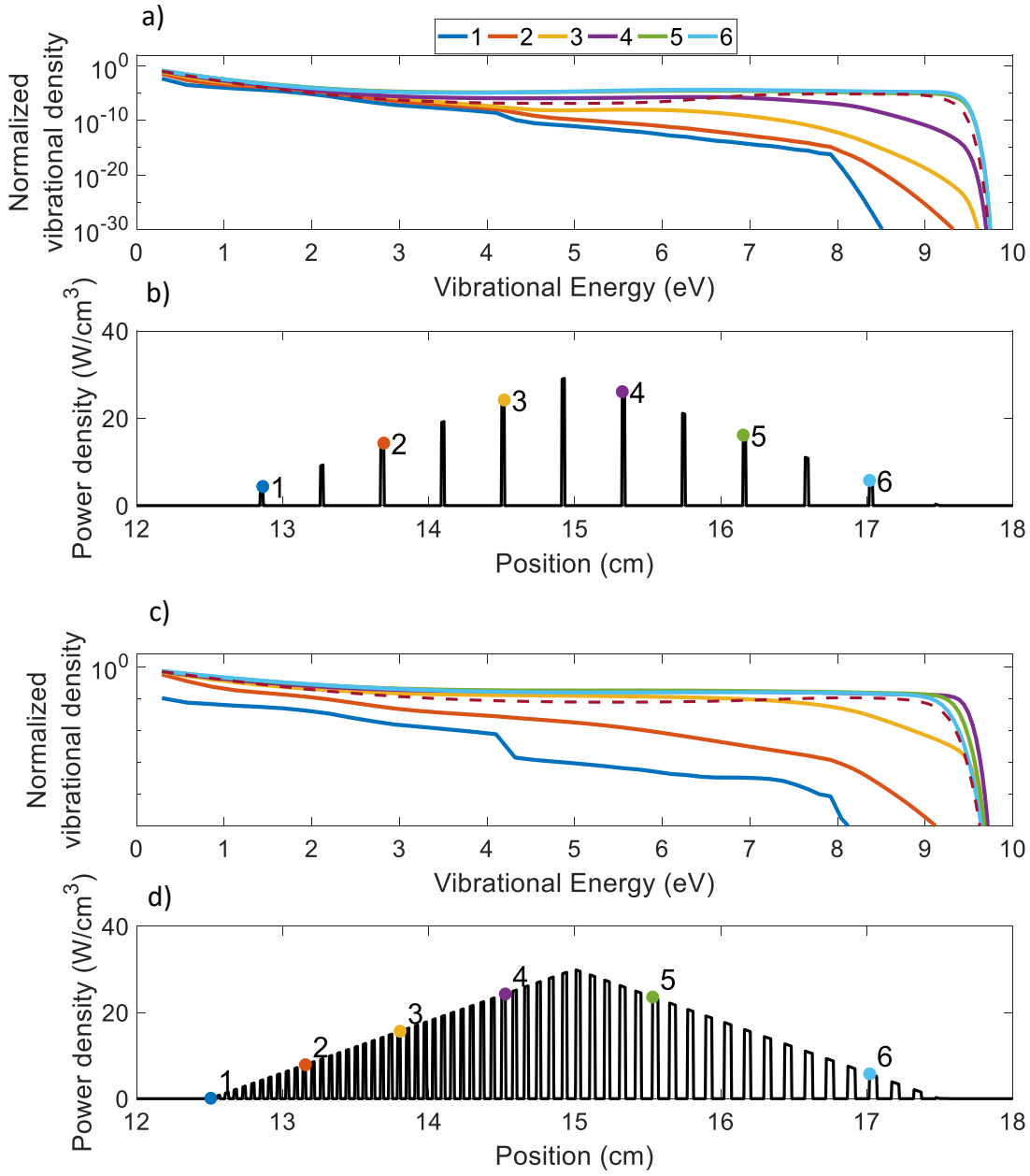

Figure 24: VDF at different positions in the plasma, for a 1000 Hz pulsed MW plasma (a) and a 7000 Hz pulsed MW plasma (c) with a pulse width of 50 µs. The locations at which the VDF's are acquired are marked with a number in the power density profile for the 1000 Hz pulse frequency (b) and 7000 Hz pulse frequency (d).

While the increasing pulse frequency promotes the occurrence of electron impact vibrational excitation processes significantly, the VV relaxation rates show a notably different trend as the pulse frequency is increased from 1000 Hz to 7000 Hz in figure 24. The 1000 Hz regime shows negative VV relaxation rates during every pulse, indicating that during the pulse on-time VV relaxation is depopulating the vibrational levels. The 7000 Hz regime on the other hand presents VV relaxation rates that eventually become positive during every pulse, pumping vibrational energy up the vibrational ladder during the pulse on-time. This demonstrates an important

distinction between high and low frequency regimes: when a pulse occurs VV relaxation processes populate higher vibrational levels in high frequency regimes, but depopulate vibrational levels in low frequency regimes. The excessive vibrational excitation, as well as the upward VV relaxation in high frequency regimes, explain the higher vibrational temperatures that are observed when the pulse frequency is increased.

Comparing the VT reaction rates at 1000 Hz and at 7000 Hz in figure 23 shows that besides the vibrational excitation, the VT relaxation processes also increase significantly in high frequency regimes. The rate profile in figure 23 clearly shows how the VT relaxation rate in the 7000 Hz regime raises to higher values much earlier in the plasma than observed in the 1000 Hz regime. These higher rates indicate that more vibrational energy is wasted in to gas heating in these higher frequency regimes, explaining the higher gas temperatures that were observed. We can thus conclude that the advantage of a pulsed regime, to supress long time scale relaxation processes, will fade away when reaching very high frequencies. Indeed, since computer calculations already pointed out that VT rates increase drastically upon rising temperature[20], the self-accelerating effect that is induced by significant VT relaxation will eventually nullify the advantages of a pulsed regime at high frequencies.

The observations demonstrating that VT relaxation becomes more significant at higher pulse frequencies, suggest that at some point a high pulse frequency will be unfavourable for the non-equilibrium in the plasma. The extent to which this occurs for the regimes studied here, will be examined. Thermal non-equilibrium is defined based on the difference between vibrational and gas temperature, so the ratio between the vibrational and gas temperature can be used as a measure for the non-equilibrium. This ratio, obtained from the experimental temperature profiles as a function of time within one pulse, is plotted in figure 25, for the four different applied frequencies. Overall, the 5000 Hz regime has achieved the highest degree of non-equilibrium, as it allows the gas to be exposed long enough to the MW radiation to achieve high vibrational temperatures through vibrational excitation, and at the same time, it is not too high for VT relaxation to significantly accelerate itself, as observed at 7000 Hz. Hence, at this frequency a perfect balance is achieved.

The ratios of vibrational and gas temperature, obtained from the 0D model, averaged over the plasma, are plotted in figure 26. These values predict that a pulse frequency of 2000 Hz delivers the perfect balance between vibrational excitation and VT relaxation. While this prediction deviates from the experimental observation, the 2000 Hz regime also has proven to deliver a significant non-equilibrium in figure 25. To some extent, the model can thus be used to evaluate

the non-equilibrium of the pulsed plasma. The disparities from the experimental non-equilibrium ratios are probably due to the differences in the calculated temperatures shown in figure 22.

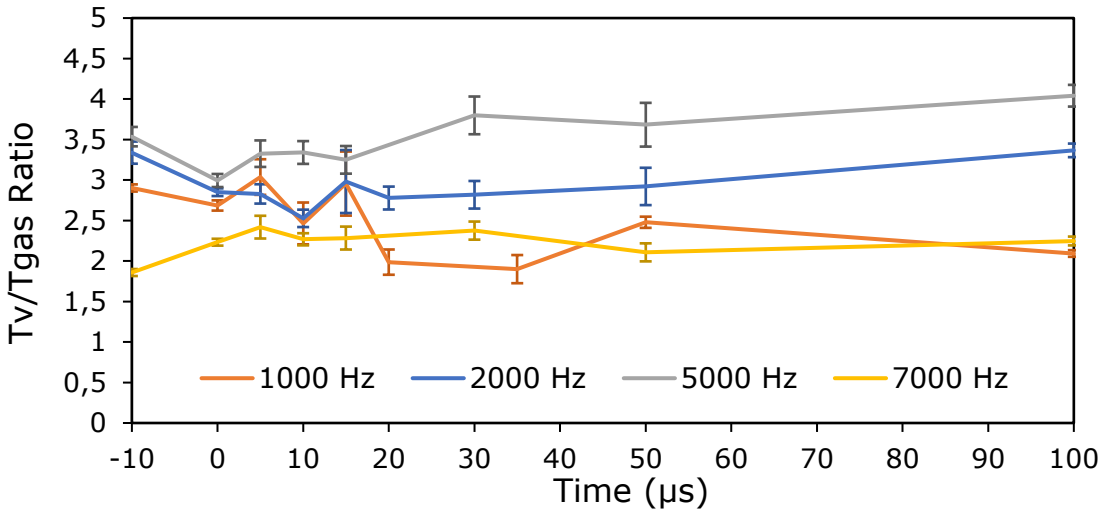

Figure 25: Ratio of Tv/Tgas, as a measure for the degree of non-equilibrium, throughout a 50 µs pulse, for 1000 Hz, 2000 Hz, 5000 Hz and 7000 Hz, obtained from the experimental temperature profiles.

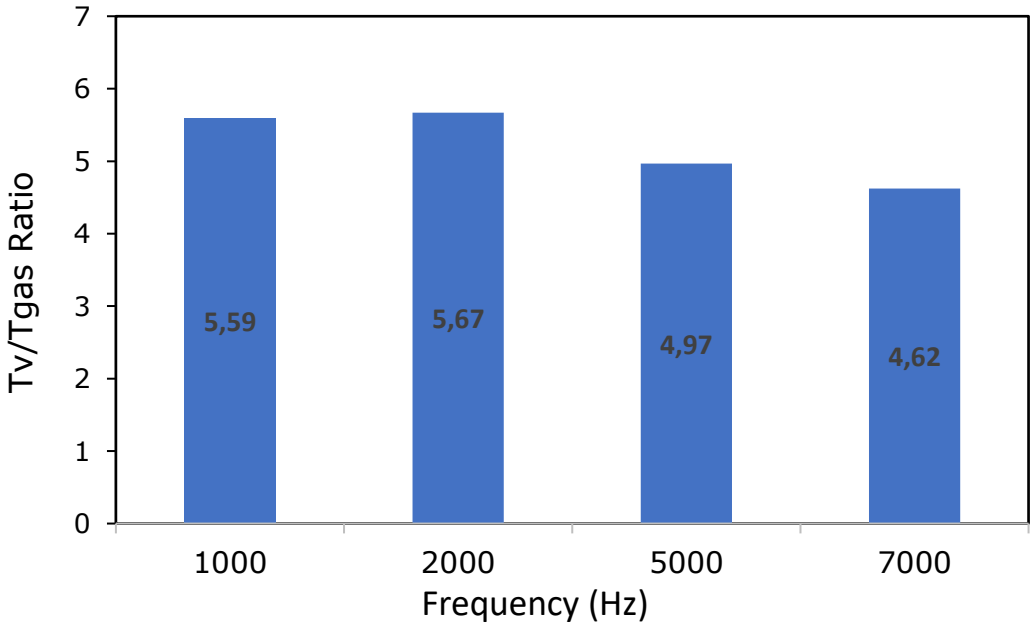

Figure 26: Ratio of Tv/Tgas, as a measure of the degree of non-equilibrium, for 1000 Hz, 2000 Hz, 5000 Hz and 7000 Hz, averaged over the whole plasma, obtained from the calculated temperature profiles.

Given the aim of this research to eventually dissociate and fix N_2, the question arises to which extent this can be achieved in the pulsed MW regimes under study. Since only pure N_2 is used

in this study, no real N_2 fixation is achieved during the experiments. For N_2 to be fixed in a stable product, the N_2 dissociation needs to be followed up by a reaction with an oxygen or hydrogen source, to form either NO_x or NH_3 (or related products), respectively. However, the dissociation to atomic N can serve as an approximative indication to the amount of N_2 that can be fixed using the pulsed regimes studied in this thesis. To calculate this approximative conversion, the N density throughout the plasma tube is calculated using the 0D model. The model determines the density through equation 6, taking into account all atomic N source processes like vibrational assisted dissociation and electron impact dissociation as well as the atomic N loss processes like N-N recombination. The resulting atomic N density profile is presented in figure 27 for the different pulse frequencies.

Given the instability of atomic N, all N atoms will eventually convert back to N_2 by recombination reactions. We therefore plot the N density at a fixed point in figure 27, which is chosen to be right after the plasma at 17.5 cm, to calculate and compare the conversions achieved in the different frequency regimes. The calculated absolute conversions at 17.5 cm are presented with the blue bars of figure 28. Evidently these absolute conversions rise with higher pulse frequency, as increasing the number of pulses inevitably means that more power is invested in the plasma. For this reason, the calculated conversions are divided by the total power that was applied to the plasma, thus taking into account the energy efficiency of the pulsed regime. These values are presented by the orange bars in figure 28. From these conversions-power ratio it is shown that, the 2000 Hz plasma delivers the highest energy efficiency. Interestingly, this is also the regime in which the most pronounced non-equilibrium is predicted by the model in figure 26. Wasting as little power as possible to gas heating during the vibrational excitation and maintaining a non-equilibrium is indeed observed to be beneficial for the conversion-energy cost ratio of the fixation process.

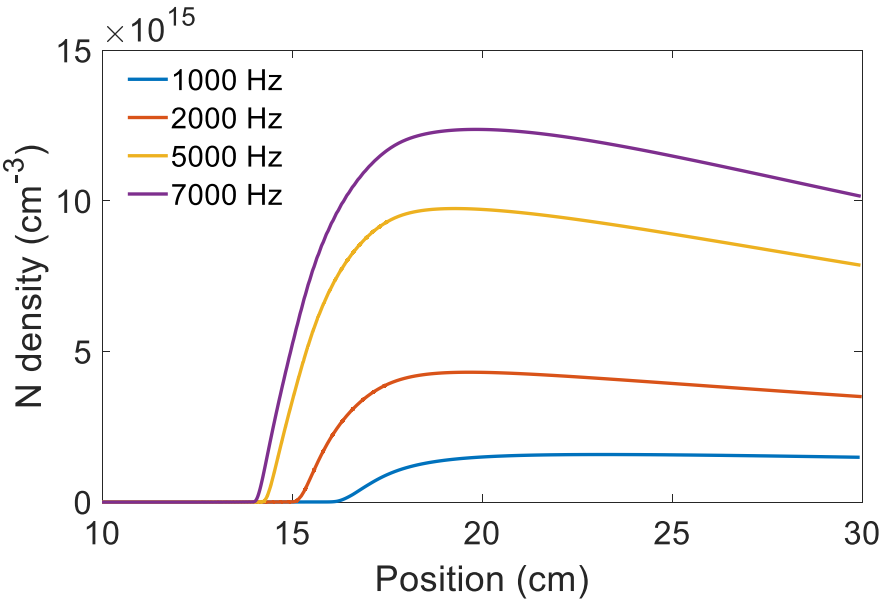

Figure 27: Calculated N density throughout the plasma tube, in a 1000 Hz, 2000 Hz, 5000 Hz and 7000 Hz pulsed MW regime.

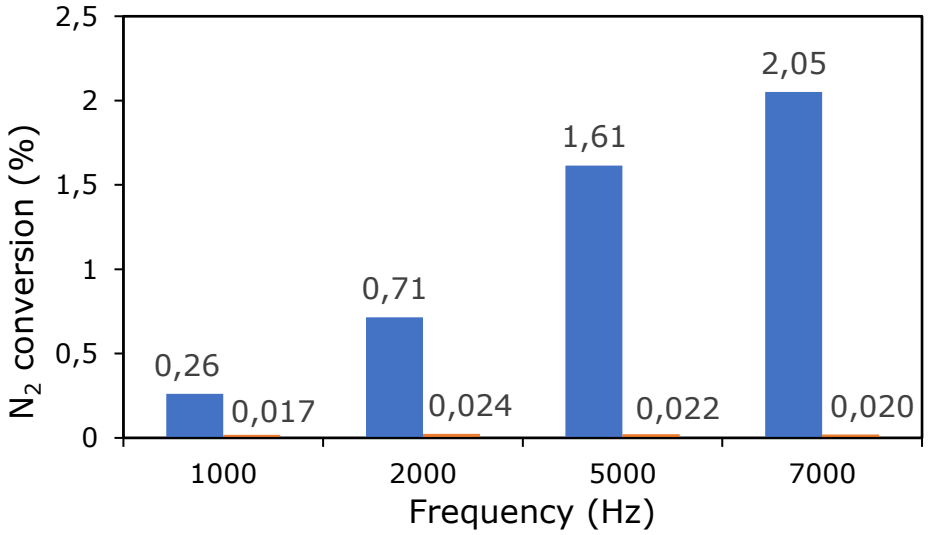

Figure 28: N_2 conversions achieved in a 1000 Hz, 2000 Hz, 5000 Hz and 7000 Hz pulsed MW plasma regime. The blue bars present the absolute conversions, the orange bars the conversions relative to power put in the plasma, serving as a measure for the energy efficiency.

The achieved performances of these pulsed MW plasmas can also be compared to conversions achieved in other plasma reactors, obtained from literature. As stated above, these conversions are based solely on the N_2 dissociation, but a comparison with literature can still be very interesting. The conversions obtained in this study are significantly higher than the observed conversion of 0.6% to NO_x in a continuous MW reactor with a comparable power density. [32] They are more comparable to the maximum observed conversion of 2% to NO_x in a gliding arc

reactor[18] or the 1,2% conversion to NH_3 observed in a catalytic DBD reactor with functionalised carbon coatings[33]. This demonstrates the potential of these high frequency pulsed MW regimes.

4.3 Variation of the pulse length

All results in the previous section were obtained using a constant pulse width of 50 µs. However, just like the pulse frequency, the pulse width also defines the amount of power that is applied to the plasma and will thus also have an impact on the vibrational excitation process. The pulse width is thus potentially a very decisive parameter for the non-equilibrium behaviour of the plasma, which is why, in this section, the effect of the pulse width will be investigated. To achieve this, the pulse frequency is fixed at 1000 Hz, while the pulse width is changed as 10, 50, 200 and 400 µs.

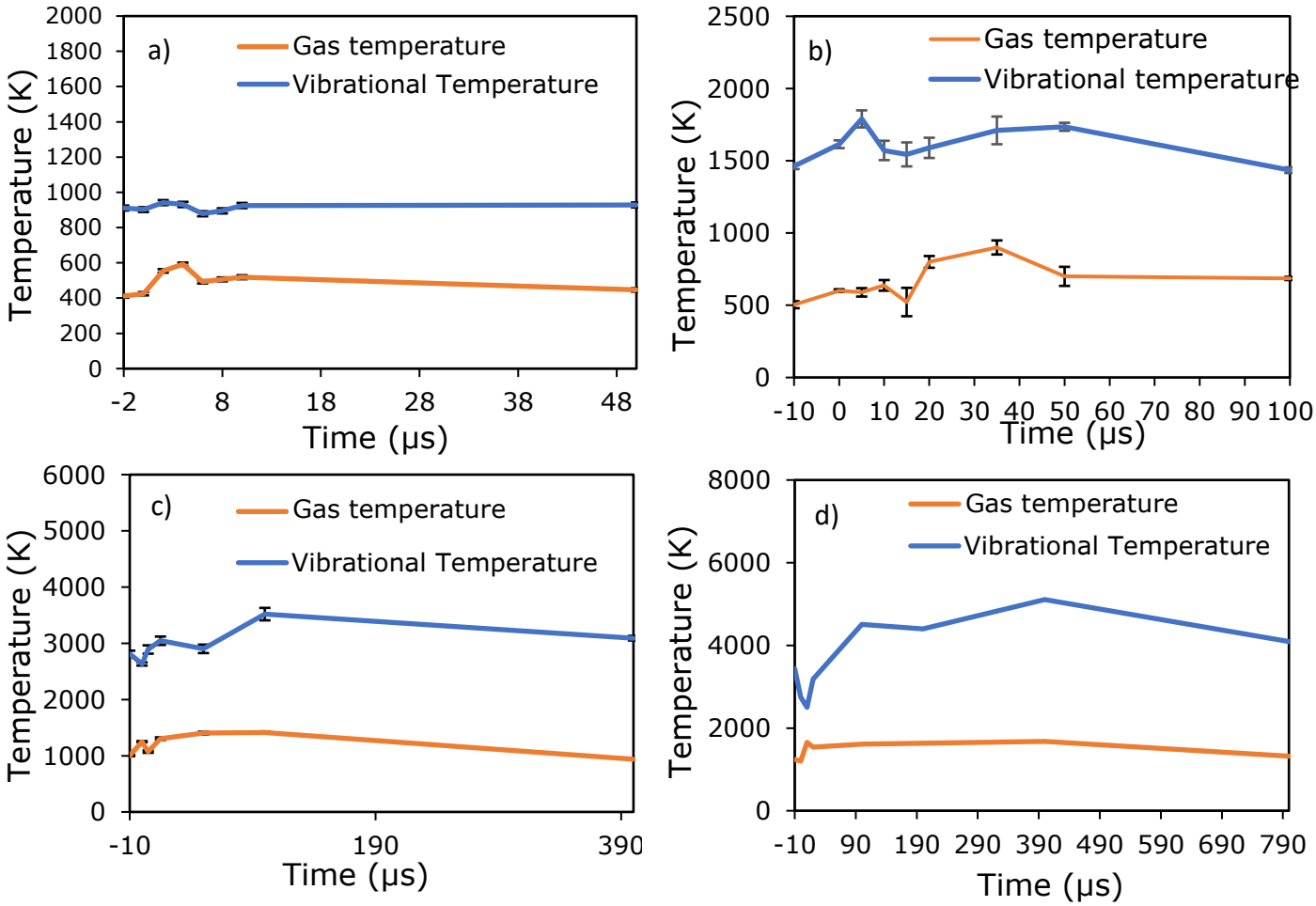

Figure 29: Experimental vibrational and gas temperature profiles throughout one pulse, with pulse width of 10 µs (a), 50 µs (b), 200 µs (c), and 400 µs (d), for a pulse repetition frequency of 1000 Hz.

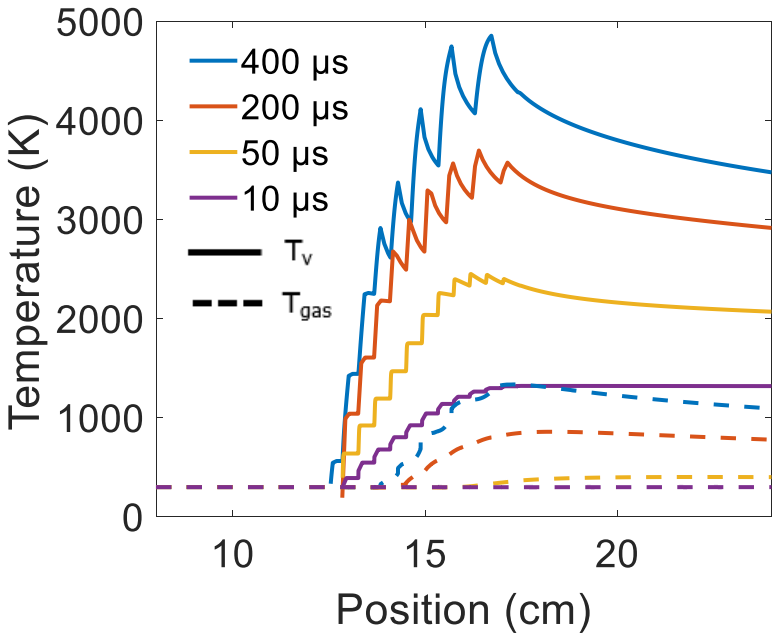

Figure 30: Calculated vibrational (full lines) and gas temperature (dashed lines) profile in a 10 µs, 50 µs, 200 µs and 400 µs pulsed MW plasma, at a pulse frequency of 1000 Hz.

The experimental vibrational and gas temperature profiles over one pulse, with pulse width of 10 µs, 50 µs, 200 µs and 400 µs, are presented in figure 29. Again these experimental temperature profiles present an averaged profile for all the pulses that the gas experiences when flowing through the plasma. In this figure, the temperature profile of the 50 µs pulse is the same as shown earlier in figure 16. The Raman spectra from which these temperatures are extracted, as well as the measured power profiles are added to the Appendix. From these temperature profiles it is very clear that the vibrational and gas temperature both increase upon increasing the pulse width. For a very short pulse width of 10 µs, there is barely any vibrational excitation, yielding a vibrational temperature below 1000 K. Hence, for a pulsed MW plasma, a pulse width of 10 µs is deemed extremely short. Referring to the one pulse experiment of section 4.1 above, the first 10 µs in the pulse yielded no significant vibrational excitation (cf. the temperature profile in figure 10 and the Raman spectrum in figure 11). The advantage of pulsing to support non-equilibrium in the MW plasma is thus observed to have a lower limit, which seems to be reached when applying a 10 µs pulse. A high pulse width like 400 µs on the other hand, demonstrates both a very high vibrational temperature and gas temperature, indicating that a high pulse width, just like a high pulse frequency, promotes both vibrational excitation

as well as heating mechanisms like VT relaxation. This trend is also clearly observed in the calculated temperature profiles in figure 30. Similar to the influence of the pulse frequency, a high pulse width causes the vibrational temperature to decline near the end of the plasma, which in turn, is accompanied by a significant raise in gas temperature. When comparing the calculated and measured averaged temperatures in figure 31, we can conclude that the values for the vibrational temperatures are again in good agreement, while the calculated gas temperatures are again underestimated, although they exhibit the same rising trend as a function of the pulse width as in the experiment.

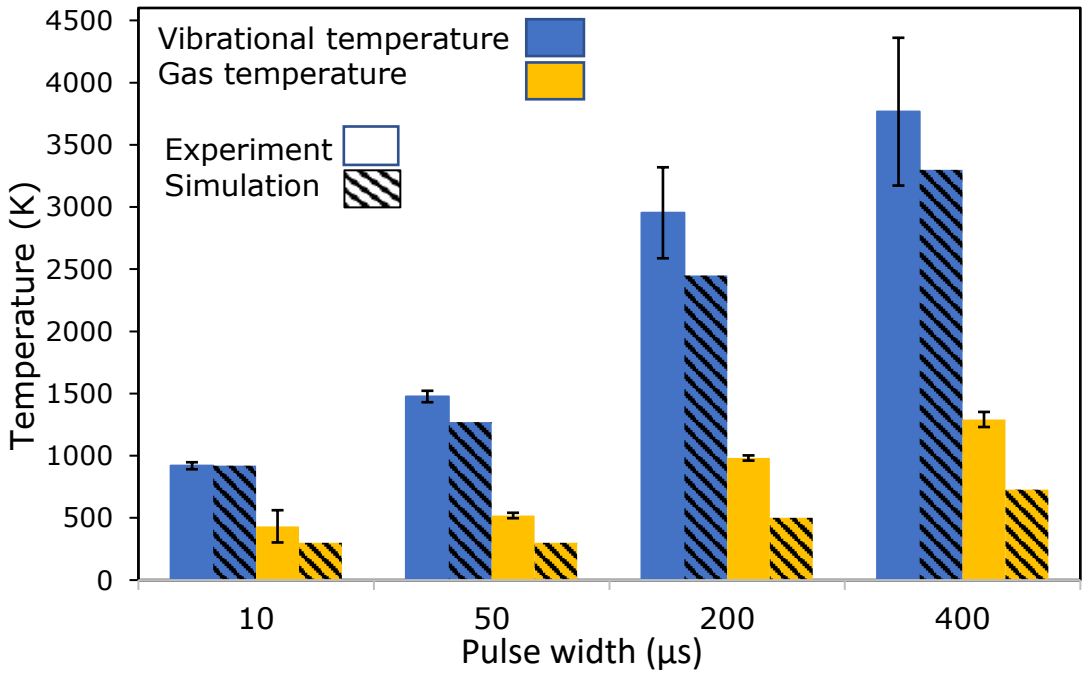

Figure 31: Calculated and measured averaged vibrational and gas temperatures, for pulse widths of 10 µs, 50 µs, 200 µs and 400 µs, at a pulse repetition frequency of 1000 Hz.

The observations that a high pulse width has a similar effect on the vibrational excitation mechanisms as a high pulse frequency, is validated by the reaction rate profiles of the 400 µs pulse in figure 32. The figure shows the reaction rate for electron impact vibrational excitation, VV and VT relaxation trough the plasma and afterglow. To have a clear view of the development of the VT relaxation rates, these reaction rates are plotted separately in figure 32b. Again, the reaction rates from all 67 vibrational levels were summed and multiplied with the energy difference of the transition (cf. above). The profiles clearly demonstrates that these long pulses give electron impact vibrational excitation reactions the opportunity to occur for a long

period of time, explaining the high vibrational temperature in this regime. However, the long exposure to the MW power during one pulse also has a clear impact on the behaviour of the relaxation processes. Both the VV and VT rates build up very fast as the pulse progresses, reaching very high rates at the end of each pulse. While high, positive VV relaxation rates are beneficial for the non-equilibrium, the high VT relaxation is not. The VT relaxation process building up inside the pulse demonstrates the longer time scale at which this relaxation process occurs. The 400 µs pulse studied here is clearly too long to take advantage of this longer timescale to supress the VT relaxation, which is why significant gas heating occurs in this regime. The extent to which this significant gas heating is deterring for the non-equilibrium is deduced from the measured and calculated ratios of T_v/T_{gas} for the different pulse widths, in figure 33 and 34, respectively.

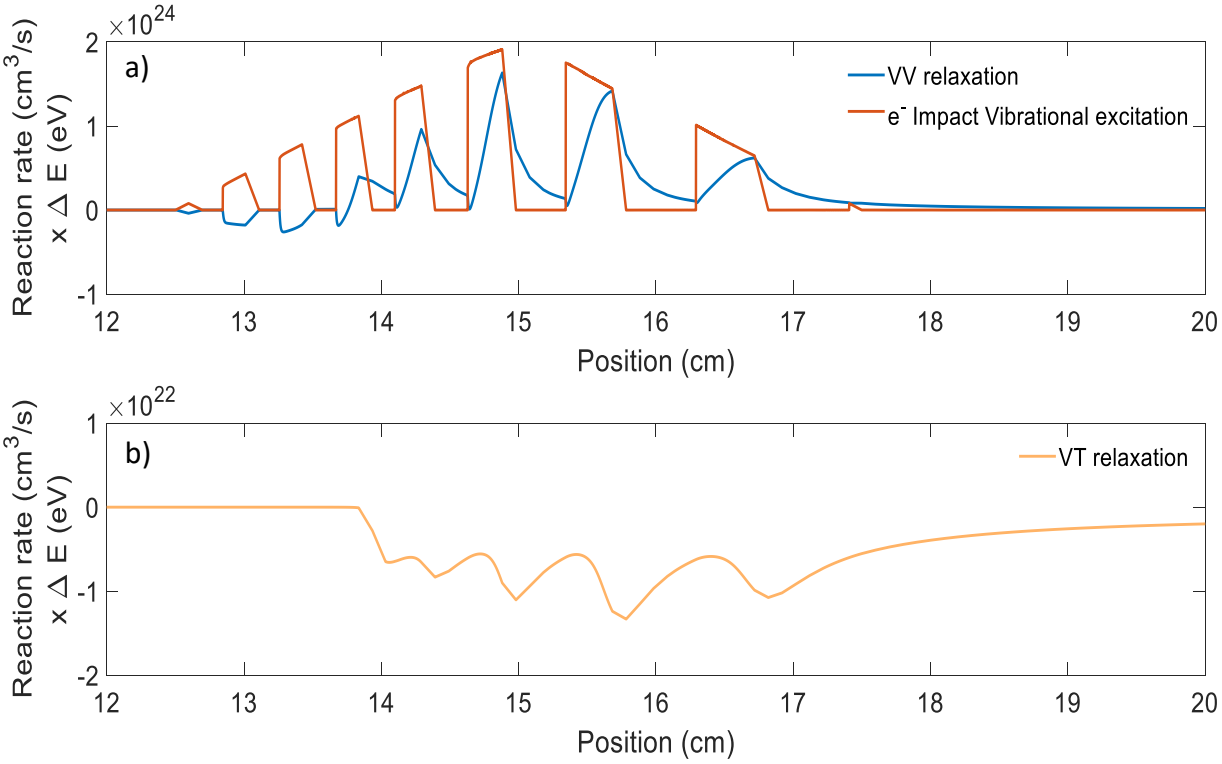

Figure 32: Reaction rate profile of the electron impact excitation and VV relaxation (a) and VT relaxation (b) through a 400 µs pulsed MW plasma. The reaction rates from all 67 vibrational levels were summed and multiplied with the energy difference of the transition.

Figure 33 shows that the pulsed MW plasmas with a longer pulse width of 200 µs and 400 µs do not provide a significantly more pronounced non-equilibrium than the 50 µs pulse regime. Although they implement a long excitation time for vibrational ladder climbing, the significant gas heating compensates for the additional vibrational excitation that occurs. As these longer

pulses put more power in the plasma, a 50 µs pulse width seems to be the more energy efficient method to achieve a pronounced non-equilibrium.

The very same trend is provided by the calculated T_v/T_{gas} ratios in figure 34. While the exact values of these ratios are a bit higher, due to the underestimated gas temperature (cf. figure 30), the trend as a function of pulse width is the same as observed in the experiment.

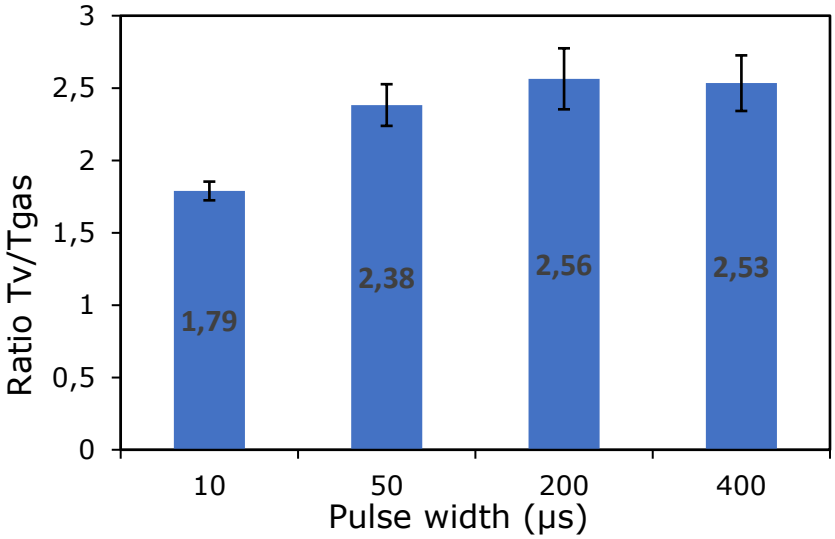

Figure 33: Experimental non-equilibrium ratios of a 10 µs, 50 µs, 200 µs and 400 µs pulsed MW plasma, all having a pulse frequency of 1000 Hz. This ratios are averaged over the whole plasma.

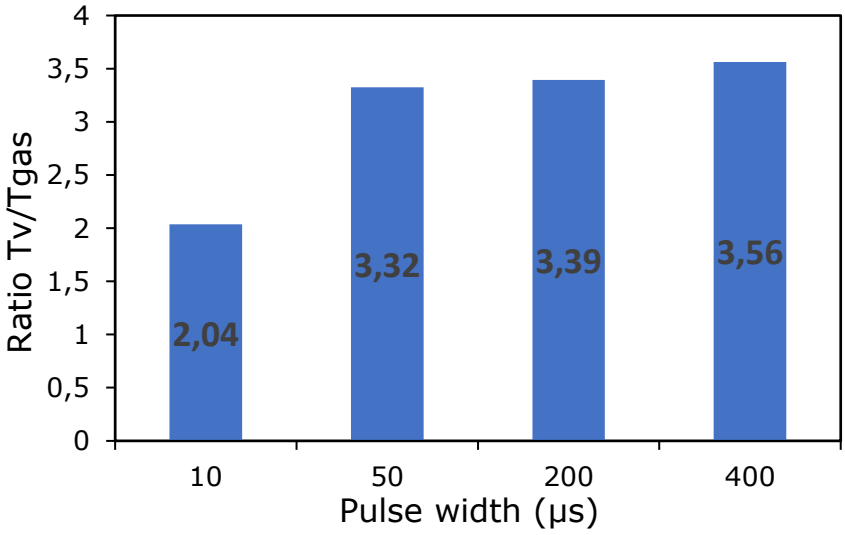

Figure 34: calculated non-equilibrium ratios of a 10 µs, 50 µs, 200 µs and 400 µs pulsed MW plasma, all having a pulse frequency of 1000 Hz. This ratios are averaged over the whole plasma.

Since the pulsed plasma regimes are aimed to be used for N_2 fixation, the effect of the pulse width on the N_2 conversion is examined. Again the dissociation to atomic N is used as an indication for the achieved conversion in the pulsed regime. The atomic N density through the

plasma and afterglow, calculated using equation 6 of the 0D model, is given in figure 35 for the four different pulse widths that were examined. Again, the atomic N density right after the plasma at 17.5 cm is used to calculate the conversions. The absolute conversions are presented in the blue bars of figure 36, while the conversions divided by the power put in the plasma, as a measure for the energy efficiency, is presented in the orange bars. The absolute conversion of 2.12 % provided by the 400 µs pulsed regime is even higher then previously observed, again proving that the performances delivered by a pulsed MW plasma are competitive with a Gliding Arc reactor (2%)[18] or a catalytic DBD reactor (1,2%)[33]. While the 400 µs pulsed regime has the highest absolute conversion, the 200 µs regime is the most energy efficient, demonstrating that the 200 µs pulse provides the optimal balance to maintain vibrational excitation processes, while still inhibiting VT relaxation. The fact that this balance is the most optimal for 200 µs pulses, was not derived from the T_v/T_{gas} ratio in figure 34. However, T_v does not deliver a complete representation of the vibrational excitation process, as it only takes the population of the first vibrational energy level into account. The energy efficiency presented in figure 36 indicates that the overall excitation process, is the most energy efficient for a 200 µs pulse regime.

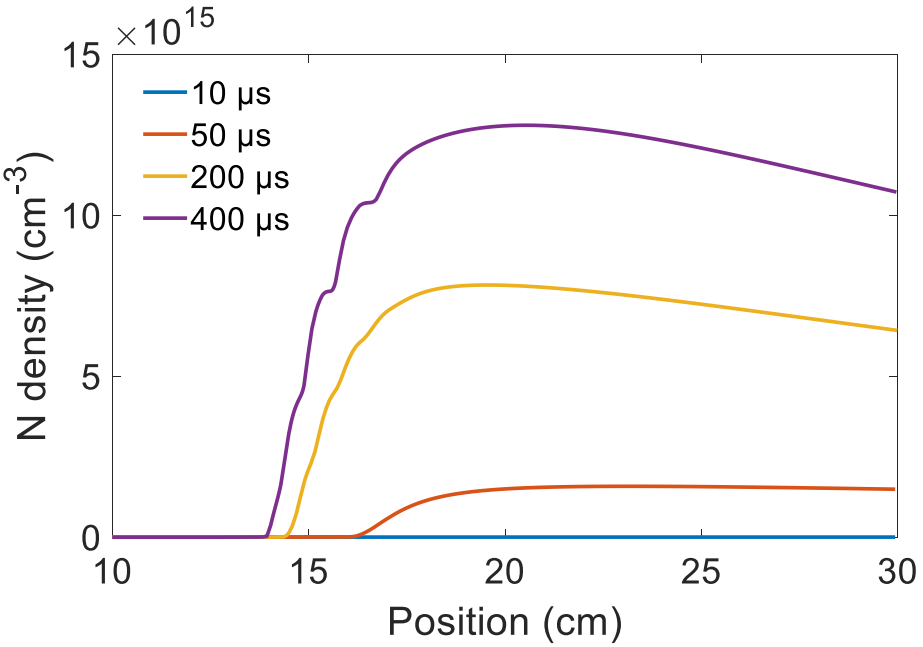

Figure 35: Calculated N density throughout the plasma tube, in a 1000 Hz, 2000 Hz, 5000 Hz and 7000 Hz pulsed MW regime.

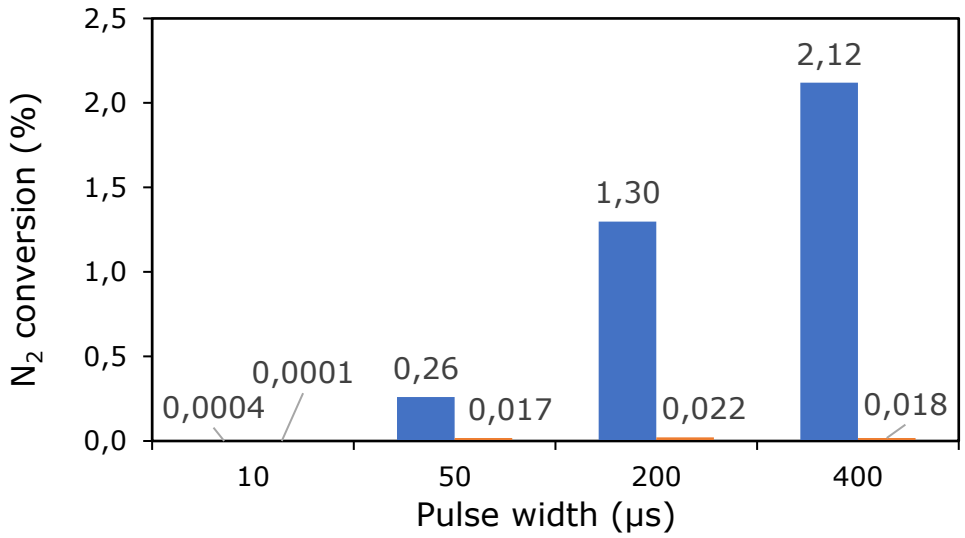

Figure 36: N_2 conversions achieved in a pulsed MW plasma regime with a pulse width of 10 µs, 50 µs, 200 µs and 400 µs. The blue bars present the absolute conversions, the orange bars the conversions relative to power put in the plasma, serving as a measure for the energy efficiency.

5. Conclusion

With the depletion of fossil fuels and global warming in prospect, this century is going to face some major energy and environmental problems. The common understanding has been developed that a transition from our carbon-based energy economy towards a sustainable one is necessary rather sooner than later. This includes an electrification of the chemical industry, as some chemical processes, like the Haber-Bosch process for ammonia production, consume 2% of the global energy production. A promising potential green alternative to the Haber-Bosch process is plasma-based N_2 fixation, for instance through pulsed MW plasmas. This master thesis attempts to gain a fundamental insight in the non-equilibrium behaviour of pulsed MW plasmas, by studying in detail the underlying processes in a single pulse, as well as the effect of the pulse frequency and pulse width on the non-equilibrium behaviour of the plasma. It is clear that a pulsed plasma takes advantage of the different time scales of the three major vibrational mechanisms in the plasma, i.e., electron impact vibrational excitation, VV and VT relaxation. By pulsing the plasma, the unfavoured VT relaxation, which operates on a long time scale, is inhibited. Through both modelling and experimental work, we identified pulse regimes with only limited VT relaxation. In these regimes, the VDF quickly reached a stationary state, at which all higher levels are overpopulated. Vibrational excitation was found to be so prominent, and VT relaxation appeared to be so low, that this characteristic shape even persisted in the afterglow. By varying the pulse parameters, it has been demonstrated that the advantage of pulsing is diminished if the frequency or the pulse length becomes too high (i.e., pulse frequency above 7000 Hz and pulse length above 400 µs). As soon as gas heating becomes too dominant, the VT rates grow rapidly, accelerating themselves even more upon gas heating. We observe that a perfect balance can be found in pulse frequency and pulse length, at which vibrational excitation occurs excessively, populating the higher vibrational levels, while the gas heating is limited. In our study, the highest non-equilibrium was achieved for a frequency of 5000 Hz and a pulse width of 50 µs, reaching a vibrational temperature of 3200 K, while the gas temperature was kept at only 900 K, yielding a very promising non-equilibrium. The various trends observed through these experiments were quite well predicted by the model. The calculated vibrational temperatures, as well as the general trends of vibrational and gas temperature as a function of the pulse operating conditions were in reasonable agreement with the experiments. Using atomic N densities provided by the model, absolute conversions around 2% are predicted, making a pulsed MW plasma competitive with other plasma reactors. While

the calculated trends were validated by the experiments, the model still has room for improvement. The gas temperatures were systematically underestimated, so there is a clear need for improving the description of the heating mechanisms. Furthermore, the fact that no Boltzmann distribution is predicted before the plasma is ignited also needs further attention. Nevertheless, the model already allows to unravel the underlying mechanisms of MW pulsed nitrogen plasmas, so an important step has been made in a better understanding of the behaviour of non-equilibrium MW plasmas.

References

(1) R. K. Pachauri and L. A. Meyer, IPCC, 2014: Climate Change 2014: Synthesis Report. Contribution of Working Groups I, II and III to the Fifth Assessment Report of the Intergovernmental Panel on Climate Change, Geneva, Switzerland, 2014.

(2) NASA. NASA Global Climate change https://climate.nasa.gov/.

(3) Prentice, I.; Farquhar, G.; Fasham, M. *Clim. Chang. 2001 Sci. Basis* **2001**, 183–237.

(4) L. Johnson, J. Grant and P. L. Low, *Two degrees of separation: ambition and reality: Low Carbon Economy Index 2014*, **2014**.

(5) Aerts, R.; Somers, W.; Bogaerts, A. *ChemSusChem* **2015**, *8*, 702–716.

(6) Whitehead, J. C. *Pure Appl. Chem.* **2010**, *82*, 1329–1336.

(7) Bogaerts, A.; Kozák, T.; van Laer, K.; Snoeckx, R. *Faraday Discuss.* **2015**, 217–232.

(8) Fridman, A. *Plasma chemistry*; 2008; Vol. 9780521847353.

(9) Bogaerts, A.; Neyts, E. C. *ACS Energy Lett.* **2018**, *3*, 1013–1027.

(10) Canfield, D. E.; Glazer, A. N.; Falkowski, P. G. *Science.* **2010**, *330*, 192–196.

(11) Aste, T. *J. Phys. Condens. Matter* **2005**, *17* , 2361–2390.

(12) Birkeland, K. *Trans. Faraday Soc.* **1906**, *2*, 98–116.

(13) Cherkasov, N.; Ibhadon, A. O.; Fitzpatrick, P. *Chem. Eng. Process. Process Intensif.* **2015**, *90*, 24–33.

(14) Patil, B. S.; Wang, Q.; Hessel, V.; Lang, J. *Catal. Today* **2015**, *256*, 49–66.

(15) Wang, Q.; Patil, B.; Anastasopoulou, A.; Butala, S.; Rovira, J.; Hessel, V.; Lang, J. *22nd Int. Symp. Plasma Chem.* **2015**, No. July, 1–2.

(16) Patil, B. S.; Cherkasov, N.; Lang, J.; Ibhadon, A. O.; Hessel, V.; Wang, Q. *Appl. Catal. B Environ.* **2016**, *194*, 123–133.

(17) Asisov, R. I.; Givotov, V. K.; Rusanov, V. D.; Fridman, A. *Sov. Phys.*, **1980**, *14*, 366.

(18) Patil, B. S.; Rovira Palau, J.; Hessel, V.; Lang, J.; Wang, Q. *Plasma Chem. Plasma Process.* **2016**, *36*, 241–257.

(19) Wang, W.; Patil, B.; Heijkers, S.; Hessel, V.; Bogaerts, A. *ChemSusChem* **2017**, *10*, 2110.

(20) Berthelot, A.; Bogaerts, A. *J. Phys. Chem. C* **2017**, *121*, 8236–8251.

(21) Asisov, R. I.; Vakar, A. K.; Jivitov, V. K.; Krotov, M. F.; Zinoviev, O. A.; Potapkin, B. V.; Rusanov, A. A.; Rusanov, V. D.; Fridman, A. A. *Proc. USSR Acad. Sci.* **1983**, *271*, 94–97.

(22) Long, D. *The Raman Effect: A Unified Treatment of the Theory of Raman Scattering by Molecules*; 202AD.

(23) Bruggeman, P. J.; Sadeghi, N.; Schram, D. C.; Linss, V. *Plasma source* **2013**, *46*.

(24) Hagelaar, G. J. M.; Pitchford, L. C. *Plasma Sources Sci. Technol.* **2005**, *14*, 722–733.

(25) IST-Lisbon database, www.lxcat.net, retrieved on May 15, **2018.**

(26) Capitelli, M.; Ferreira, C. M.; Gordiets, B. F.; Osipov, A. I. *Plasma kinetics in atmospheric gases*; 2000.

(27) Schwartz, R. N.; Slawsky, Z. I.; Herzfeld, K. F. *J. Chem. Phys.* **1952**, *20*, 1591–1599.

(28) Kozàk, T.; Bogaerts, A. *Plasma Sources Sci. Technol.* **2014**, *23*.

(29) Yan, Y.; Su, D. L. *Proc. - Asia-Pacific Conf. Environ. Electromagn. CEEM 2003* **2003**, 518–522.

(30) Capitelli, M.; Colonna, G.; D'Ammando, G.; Laricchiuta, A.; Pietanza, L. D. *Plasma Sources Sci. Technol.* **2017**, *26* (3).

(31) Ochkin, V. N. *Spectroscopy of Low Temperature Plasma*; **2009**.

(32) Kim, T.; Song, S.; Kim, J.; Iwasaki, R. *Jpn. J. Appl. Phys.* **2010**, *49*.

(33) Hong, J.; Aramesh, M.; Shimoni, O.; Seo, D. H.; Yick, S.; Greig, A.; Charles, C.; Prawer, S.; Murphy, A. B. *Plasma Chem. Plasma Process.* **2016**, *36* , 917–940.

(34) Nighan, W. L. *Phys. Rev. A* **1970**, *2*, 1989–2000.

(35) Linstrom, P. J.; Mallard, W. G. *NIST Standard Reference Database Number 69*; 2005.

(36) Heijkers, S.; Snoeckx, R.; Kozák, T.; Silva, T.; Godfroid, T.; Britun, N.; Snyders, R.; Bogaerts, A. *Ispc* **2015**, No. MAY, 22–24.

Appendix

1.Reactions used in the 0D model

Reaction type	Reaction	Ref
Elastic collision	$e^- + N_2 \rightarrow e^- + N_2$	Calculated by Bolsig +[24,34]
Electron impact vibrational excitation	$e^- + N_2 \rightarrow e^- + N_2(Vn)$	Calculated by Bolsig +[24,34]
Electron impact ionization	$e^- + N_2 \rightarrow e^- + N_2^+$	Calculated by Bolsig +[24,34]
Electron impact dissociation	$e^- + N_2 \rightarrow e^- + N + N$	Calculated by Bolsig +[24,34]
Electron impact excitation	$e^- + N_2 \rightarrow e^- + N_2^*$	Calculated by Bolsig +[24,34]
Dissociation metastable excited state	$e^- + N_2^* \rightarrow e^- + N + N$	Calculated by Bolsig +[24,34]
Vibrational induced dissociation	$N_2(Vn) + M \rightarrow N+N+M$	[35]
Recombination	$N+N+M \rightarrow N_2+M$	[35]
Three body recombination	$N+N+N \rightarrow N_2+N$	[36]
VT relaxation	$N_2(Vn) + M \rightarrow N_2(Vn-1) + M$	[26]
VV relaxation	$N_2(Vn)+ N_2(Vm) \rightarrow N_2(Vn+1)+ N_2(Vn-1)$	[26]

Backward reaction rates are calculated following the principle of detailed balance

2. Raman spectra

In this section, the measured power pulse profile as well as an exemplary Raman spectrum is shown for each of the examined experimental conditions. All spectra are recorded at a flow rate of 4 slm and a pressure of 25 mbar.

One pulse regime (30 Hz), Raman spectrum at 60 µs:

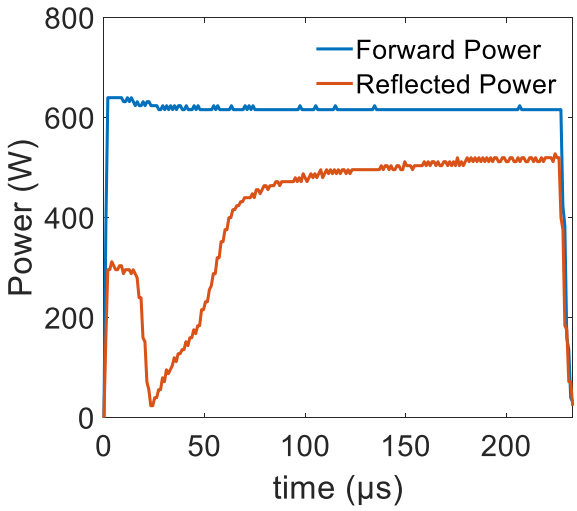

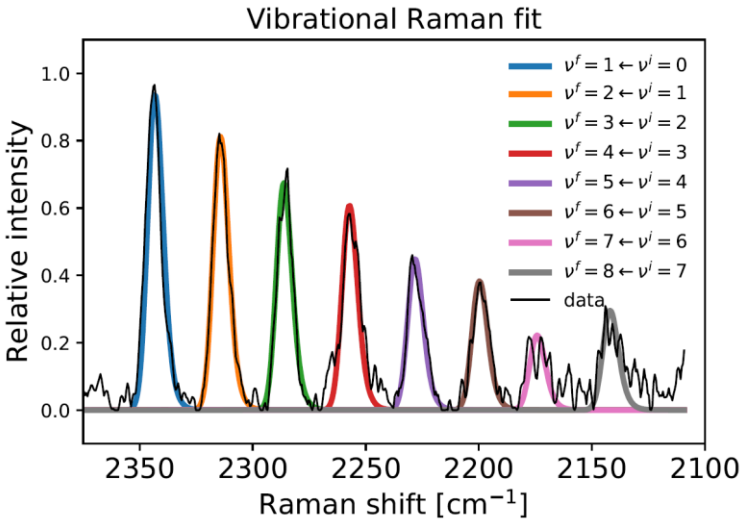

1000 Hz regime, 50 µs pulse width, Raman spectrum at 30 µs:

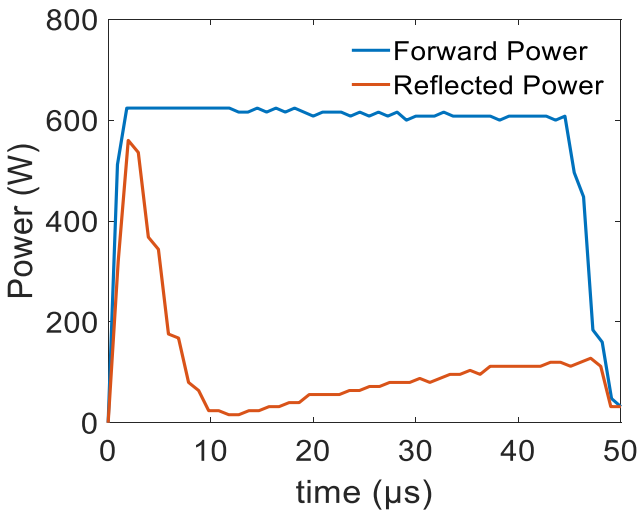

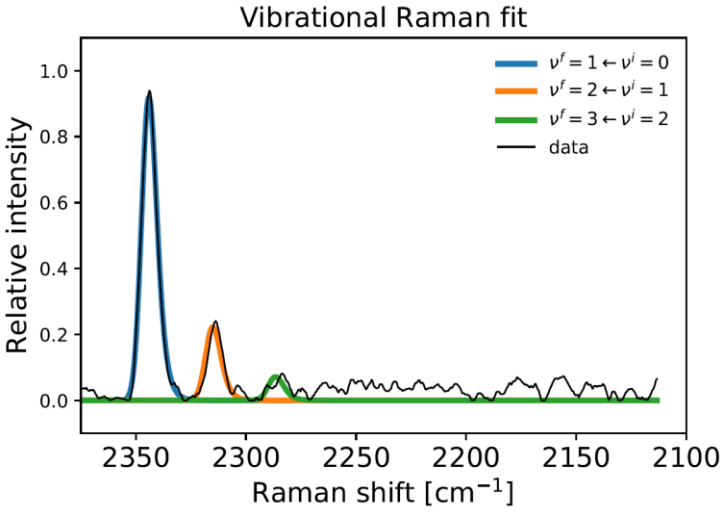

2000 Hz regime, 50 µs pulse width, Raman spectrum at 30 µs:

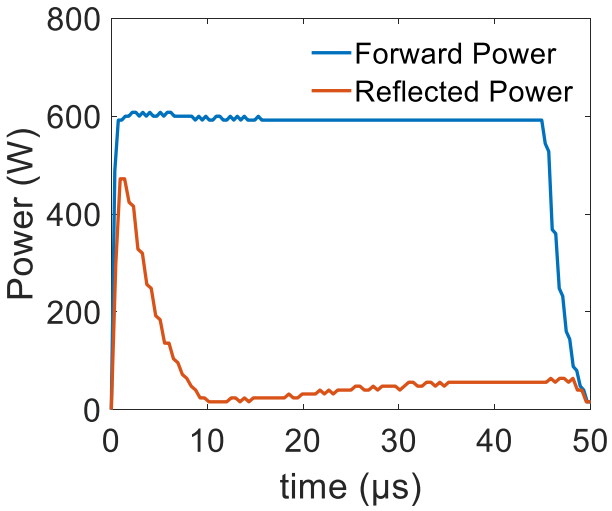

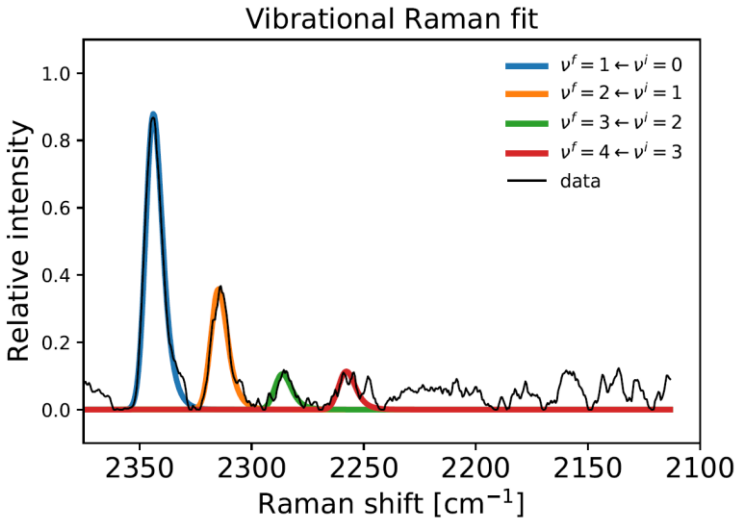

5000 Hz regime, 50 µs pulse width, Raman spectrum at 30 µs:

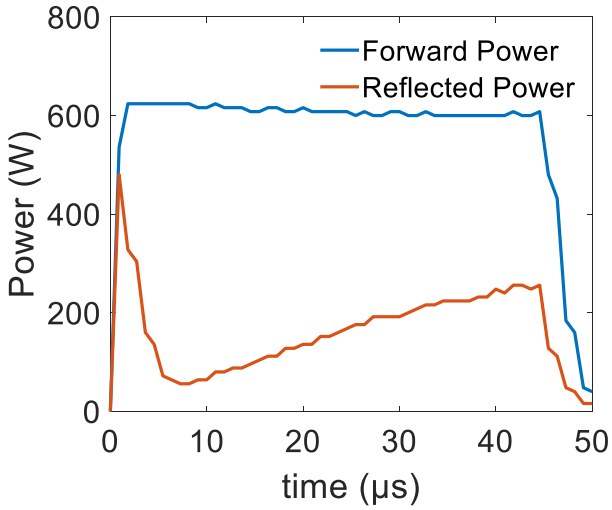

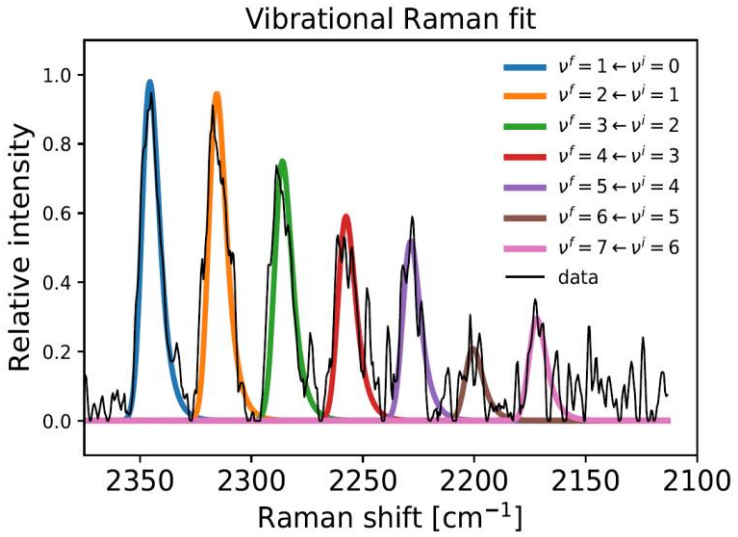

7000 Hz regime, 50 µs pulse width, Raman spectrum at 30 µs:

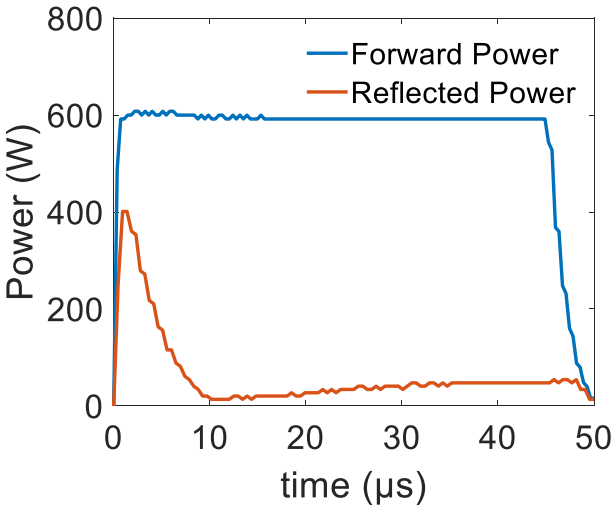

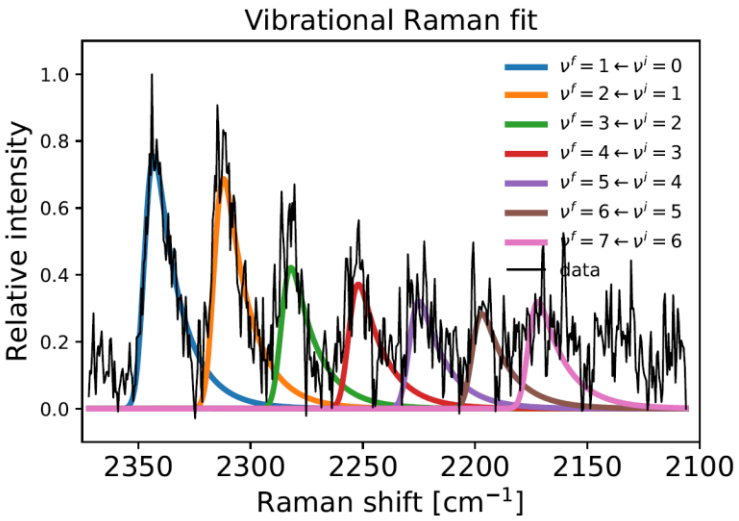

1000 Hz regime, 10 µs pulse width, Raman spectrum at 6 µs:

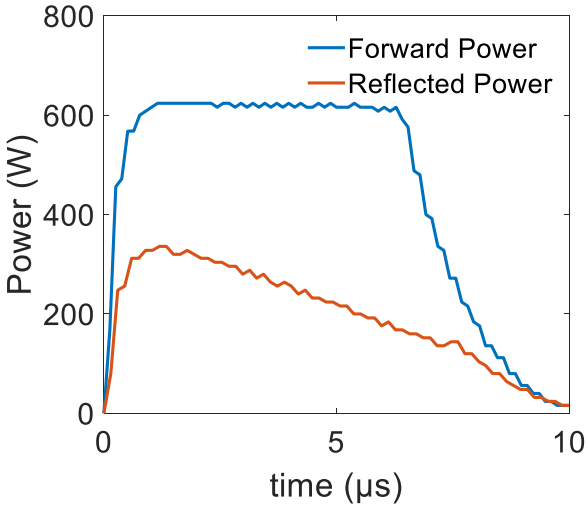

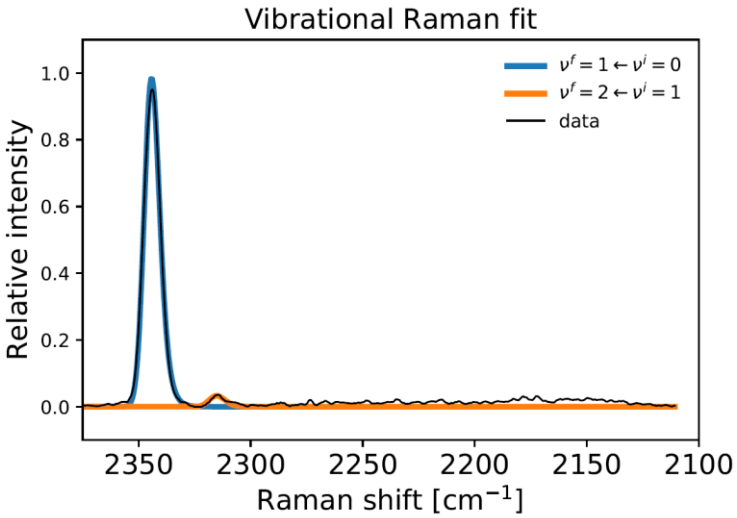

1000 Hz regime, 200 µs pulse width, Raman spectrum at 50 µs:

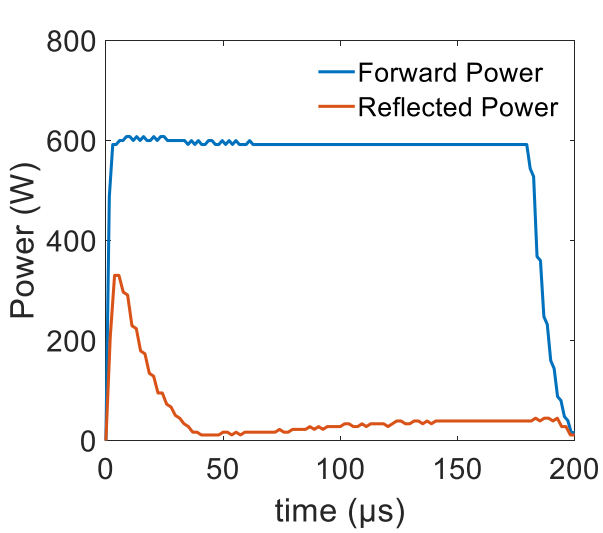

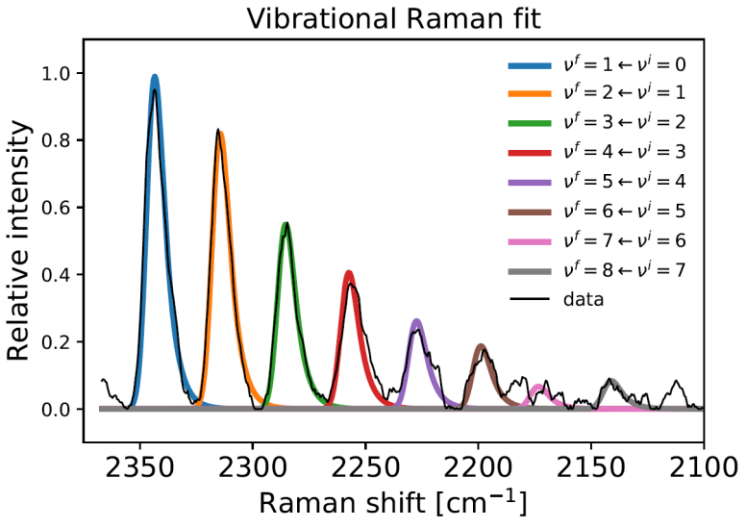

1000 Hz regime, 400 µs pulse width, Raman spectrum at 200 µs :